

Sublithosphere mantle crystallization and immiscible sulphide melt segregation in continental basalt magmatism: evidence from clinopyroxene megacrysts in the Cenozoic basalts of eastern China

Pu Sun^{1,2*}, Yaoling Niu^{2,3,4}, Pengyuan Guo^{1,2}, Meng Duan^{1,2}, Xiaohong Wang^{1,2}, Hongmei Gong^{1,2}

¹Key Laboratory of Marine Geology and Environment, Institute of Oceanology, Chinese Academy of Sciences, Qingdao 266071, China.

²Laboratory for Marine Geology, Qingdao National Laboratory for Marine Science and Technology, Qingdao 266061, China.

³Department of Earth Sciences, Durham University, Durham DH1 3LE, UK.

⁴School of Earth Science and Resources, China University of Geosciences, Beijing 100083, China.

Correspondence:

Pu Sun (pu.sun@qdio.ac.cn)

ABSTRACT

This study explores the effects of high-pressure crystallization and immiscible sulphide melt segregation under mantle conditions on the compositional variation of basaltic magmas, using clinopyroxene megacrysts in the Cenozoic basalts of eastern China. These clinopyroxene megacrysts are large (up to > 10 cm in size) and homogeneous at the grain scale. They were crystallized from variably evolved parental magmas and then captured by their host basalts. The large and systematic variations of $[\text{Sm}/\text{Yb}]_{\text{N}}$, Lu/Hf, Fe/Mn, Sc/La, Ni and Cu with $\text{Mg}^{\#}$ in the clinopyroxene megacrysts suggest their co-precipitation with garnet and with immiscibility between sulphide and silicate melts. This is consistent with the appearance of garnet megacrysts in the host basalts and abundant sulphide globules in the clinopyroxene megacrysts. The covariation between Ni contents of sulphide globules and $\text{Mg}^{\#}$ of the clinopyroxene megacrysts suggests a genetic relationship between sulphide globules and clinopyroxene megacrysts. High-pressure crystallization of clinopyroxene and garnet results in decrease of $\text{Mg}^{\#}$ and concentrations of CaO, MnO and heavy rare earth elements (e.g., Yb) and increase of Fe/Mn and $[\text{Sm}/\text{Yb}]_{\text{N}}$ in the residual melts. Therefore, geochemical characteristics of low $\text{Mg}^{\#}$, low CaO and MnO contents and high Fe/Mn and $[\text{Sm}/\text{Yb}]_{\text{N}}$ in basalts do not necessarily indicate a pyroxenite mantle source. In addition, caution is needed when applying the olivine addition method to infer the primary compositions of alkali basalts without considering the effects of high-pressure crystallization of clinopyroxene and garnet. The calculated P - T conditions of

the clinopyroxene megacrysts are close to those of the lithosphere-asthenosphere boundary (LAB) beneath eastern China, and the low primitive $[\text{Sm}/\text{Yb}]_{\text{N}}$ (~ 4.0) of melts parental to the clinopyroxene megacrysts suggests final equilibration at relatively low pressures most likely beneath the LAB. Hence, a melt-rich layer is expected close beneath the LAB. Melt pools in this melt-rich layer provide a stable and closed environment for the growth of compositionally homogeneous clinopyroxene megacrysts. As a result, melts in these melt pools are compositionally evolved with low and variable $\text{Mg}^{\#}$. Subsequent pulses of melt aggregation/supply from depths with primitive compositions and high $\text{Mg}^{\#}$ will disturb these melt pools, cause magma mixing and trigger the eruption of magmas carrying clinopyroxene and garnet megacrysts.

Key words: Cenozoic basalts in continental eastern China; Clinopyroxene megacryst; High-pressure crystallization; Lithosphere-asthenosphere boundary; Immiscibility between sulphide and silicate melts

INTRODUCTION

The compositions of mantle-derived magmas are used to infer melting conditions, mantle compositions and source lithologies (e.g., Sobolev et al., 2005, 2007; Herzberg, 2006; Niu & O'Hara, 2008; Lee et al., 2009; Yang & Zhou, 2013). However, during magma ascent from the source region via the cold lithosphere to the surface, modification of magma compositions by fractional crystallization is inevitable because of conductive cooling to ambient wall-rocks (e.g., Green & Ringwood, 1964; O'Hara, 1965; Irving & Green, 2008; Hole, 2018; Sun et al., 2018). One may consider basalts containing mantle peridotite xenoliths to represent primary mantle-derived magmas with negligible modification by fractional crystallization because these magmas must ascend rapidly to carry physically dense xenoliths to the surface with little time for significant crystallization (see Sun et al., 2018 for discussion). However, basaltic magmas could have been compositionally evolved before mantle xenolith incorporation. For instance, highly evolved phonolites containing peridotite xenoliths have been reported worldwide, which highlights the importance of high-pressure crystallization of basaltic magmas before mantle xenolith incorporation and rapid eruption (Green et al., 1974; Irving & Price, 1981; Irving & Green, 2008; Price & Green, 1972; Wright, 1966). Therefore, the effect of high-pressure fractional crystallization, even for mantle xenolith-bearing basalts, on bulk-rock compositions must be assessed before using basalt compositions to infer mantle melting conditions and source lithologies. Otherwise, the inferred mantle source information would be erroneous.

Cenozoic basalts are widespread in eastern continental China (Fig. 1). They are mainly alkali basalts (e.g., olivine nephelinites, basanites and alkali olivine basalts) and contain abundant mantle xenoliths (e.g., garnet/spinel peridotites and garnet pyroxenites). In recent years, abundant studies have suggested a pyroxenite mantle source for these basalts (e.g., Li et al., 2015; Liu et al., 2008a; Pang et al., 2019; Wang et al., 2011; Wang et al., 2015; Yang & Zhou, 2013; Yang et al., 2016; Yu et al., 2018; Zeng et al., 2013; Zhang et al., 2008; Zhang et al. 2009), mostly because these basalts show high Fe/Mn but low CaO contents, speculated to be characteristic pyroxenite-derived melts (Sobolev et al., 2005, 2007). This is because pyroxene (and also garnet) has a lower partition coefficient (K_d) for Fe/Mn and a higher K_d for CaO than olivine (Humayun et al., 2004; Herzberg, 2006; Le Roux et al., 2011; Niu et al., 2011). However, the effect of fractional crystallization (especially at high pressures) on bulk-rock compositions of these basalts has been overlooked. Crystallization of clinopyroxene + garnet from alkali basaltic magmas at high pressures has long been determined through experimental and phase equilibria studies (Yoder & Tilley, 1962; O'Hara, 1965, 1968; Bultitude & Green, 1967; O'Hara & Yoder, 1967; Green & Ringwood, 1967; O'Hara et al., 1975) and by studies on natural garnet pyroxenites (Green, 1966; Frey, 1980; Sen, 1988; Sen & Jones, 1990; Bizimis et al., 2005; Keshav et al., 2007). Importantly, residual melts after fractional crystallization of clinopyroxene + garnet can have geochemical characteristics that mimic those expected for pyroxenite-derived melts (Hole, 2018). In addition, Ni contents in basalts and olivine

phenocrysts have been widely used to trace mantle source lithologies (pyroxenite versus peridotite) because pyroxenites were speculated to result from reaction of SiO₂-rich melt with peridotite and total olivine consumption (Sobolev et al., 2005, 2007). Consequently, the pyroxenite-derived melts have higher Ni contents than peridotite-derived melts (Sobolev et al., 2005, 2007). However, Ni contents in basalts (and thus in olivine phenocrysts crystallized from basalts) can easily be modified by fractional crystallization of olivine and clinopyroxene and immiscible fractionation of sulphides during magma evolution (Bézos et al., 2005; Czamanske & Moore, 1977; Keays, 1995; Yang et al., 2014).

In this paper, we discuss crystallization of clinopyroxene and garnet and concurrent immiscible fractionation of sulphide melts at sub-lithosphere mantle conditions using Cenozoic basalts and clinopyroxene megacrysts in eastern China. Because fractional crystallization of clinopyroxene and garnet could result in high Fe/Mn and Sm/Yb and low CaO contents in the residual melts, these geochemical characteristics of basalt samples should not be used indiscriminately as evidence for a garnet pyroxenite mantle source.

PETROLOGICAL CHARACTERISTICS

Cenozoic basalts in eastern China contain abundant megacrysts mainly of clinopyroxene (Fig. 2a), lesser amounts of garnet (Fig. 2b) and rare zircon, mica, amphibole, ilmenite and plagioclase (Liu et al., 1992; Sun et al., 2020; Xu et al., 1998; Yu et al., 2019; Zhi et al., 1990). Black clinopyroxene and red garnet megacrysts appear

in various sizes (from ~ 1 cm to > 10 cm) (Figs. 2a-c) and usually occur with mantle peridotite xenoliths (Fig. 2c). The clinopyroxene megacrysts are particularly interesting with a “glassy” luster, anhedral shape and a conchoidal fracture (Fig. 2a). They are optically homogeneous with thin reaction rims (Fig. 2d). Some of them show first-order interference color (vs. second-order interference colors for all the common and familiar clinopyroxene crystals) (Fig. 2d). Abundant sulphide globules (~ 30-80 μm in diameter) are common in these clinopyroxene megacrysts (Fig. 2e). The globular morphology (Fig. 2f) is consistent with the sulphide being formed from immiscible liquids trapped during growth of the megacrysts (Peterson & Francis, 1977; Andersen et al., 1987). Trails of tiny sulphide grains extending out of the large one are observed (Fig. 2f), which may result from the decrepitation of sulphides during rapid ascent of host magmas (Andersen et al., 1987; Harvey et al., 2016). This study collected 39 clinopyroxene megacrysts from Kuandian (n = 8), Penglai (n = 9), Dalinor (n = 14), Nanjing (n = 5), Jiucaidi (n = 1) and Yangyuan (n = 2) and 31 host basalts from Kuandian (n = 8), Penglai (n = 10), Dalinor (n = 8) and Nanjing (n = 5).

ANALYTICAL METHODS

LA-ICP-MS analyses

Major and trace elements of 33 clinopyroxene megacrysts were analyzed in thin (~ 60 μm) sections using laser-ablation inductively coupled plasma mass spectrometry (LA-ICP-MS) in the Laboratory of Ocean Lithosphere and Mantle Dynamics, Institute

of Oceanology, Chinese Academy of Sciences. Laser sampling was performed using a Photon Machines Excite 193 nm excimer Ar-F laser system, and an Agilent 7900a ICP-MS instrument was used to acquire ion-signal intensities. The samples were analyzed using a 40 μm spot and 3.98 J/cm² energy density at a repetition rate of 6 Hz. Each analysis included 25 s background acquisition (gas blank) followed by 50 s data acquisition. Multiple reference materials of NIST SRM 610, GSE-1G, USGS BCR-2G, BHVO-2G and BIR-1G were used as external standards for calibration. Every five sample analyses were followed by two analyses of GSE-1G (one as QC to correct for time-dependent drift of sensitivity and the other as an unknown sample to check for analytical accuracy and precision). The raw data were processed using ICPMSDataCal (Liu et al., 2008b). Repeated analyses of GSE-1G give analytical precisions (RSD) < 1% for SiO₂, Al₂O₃ and V, 1-5% for most elements and 5-10% for Cs, Th and U and analytical accuracies (RE) within 1% for FeO, MgO, Cu, Ba, La and Sm, 1-5% for most elements, 5-10% for V, Ga, Y, Nb, Gd, Tb and Er and 10-15% for Zn and Ta. The analytical data including 199 spot analyses, with 5 to 8 points in a profile per clinopyroxene crystal, are given in Supplementary Table 1. The analytical results of reference materials are given in Supplementary Table 2. Detailed analytical methods are in Xiao et al. (2020).

Electron microprobe analyses

Major elements of 6 clinopyroxene megacrysts and sulphides in 16 clinopyroxene megacrysts were analyzed in thin (~ 30 μm) sections, using a JEOL JXA8230 electron

microprobe analyzer (EMPA) equipped with three wavelength dispersive spectrometers at the Ocean University of China. The analyses used an accelerating voltage of 15 kV and a beam current of 20 nA. For clinopyroxene analyses, a beam diameter of 5 μm was used, and the standards used for calibration include diopside for SiO_2 , MgO and CaO, rutile for TiO_2 , garnet for Al_2O_3 , haematite for FeO, bustamite for MnO, jadeite for Na_2O , sanidine for K_2O and chromium oxide for Cr_2O_3 . For sulphide analyses, beam diameters of 2-5 μm were used, and the standards used for calibration include skutterudite for As and Co, pyrite for S and Fe, galena for Pb, pentlandite for Ni, chalcopyrite for Cu and sphalerite for Zn. The analytical results include 34 spot analyses for 6 clinopyroxene megacrysts and 141 spot analyses for sulphides, which are given in Supplementary Table 1 & 3, respectively. Analytical results of the diopside standard and sulphide (pyrite, chalcopyrite, pentlandite, sphalerite) standards are given in Supplementary Table 4. Detailed analytical methods are described in [Lai et al. \(2018\)](#).

Bulk-rock major and trace element analyses

We crushed fresh basalt samples to ~ 1 mm grains to exclude phenocrysts and xenocrysts with the aim of obtaining melt compositions represented by the pure matrix. These sample grains were repeatedly washed in Milli-Q water in an ultrasonic bath and dried in a clean environment.

Major and trace elements of basalts were analyzed in the Laboratory of Ocean Lithosphere and Mantle Dynamics, the Institute of Oceanology, Chinese Academy of

Sciences. Major elements of basalt matrix were analyzed using an Agilent 5100 inductively coupled plasma optical emission spectrometer (ICP-OES). About 50 mg of sample grains and 250 mg of lithium metaborate (LiBO_2) were weighted and mixed in a platinum crucible and melted in a muffle furnace at 1050 °C for 1 h. The melt was further heated and swirled on a Bunsen burner at ~1000 °C to ensure all melt forming a coherent single drop, which was finally poured and dissolved in 5% HNO_3 . Repeated analyses of USGS reference rock standards BHVO-2 and BCR-2 give analytical precisions < 1% for SiO_2 , Al_2O_3 , FeO, MnO, MgO, CaO and Na_2O , 1-3% for K_2O and TiO_2 , and ~ 5% for P_2O_5 . Analytical accuracies of BHVO-2 are within 2% for TiO_2 , FeO, MnO, MgO, CaO, Na_2O and K_2O , and ~ 2-5% for SiO_2 , Al_2O_3 and P_2O_5 .

Trace elements of basalt matrix were analyzed using an Agilent 7900 inductively coupled plasma mass spectrometer (ICP-MS). Fifty milligrams of each sample were dissolved with an acid mix of distilled HCl, HNO_3 and HF in a high-pressure jacket equipped Teflon beaker for 15 hours, and then re-dissolved with 20% HNO_3 for 2 hours until complete digestion. Repeated analyses of USGS reference rock standards BHVO-2 and BCR-2 give analytical precisions better than 2% for most elements and ~ 2-5% for Be, Cs, Ba and U. Analytical accuracies of BHVO-2 are within 5% for most elements and 5-10% for Cr, Ni, Ga, Rb, Y, Dy and Pb. See [Chen et al. \(2017\)](#) for analytical details. The analytical results of major and trace elements in BHVO-2 and BCR-2 are given in Supplementary Table 5.

RESULTS

Clinopyroxene megacrysts

Although having variably large sizes, these clinopyroxene megacrysts are all homogenous at the individual grain scale (Supplementary Table 1). In the following, we use average composition of multiple spot analyses in each megacryst (Table 1). However, different clinopyroxene megacrysts show large compositional variations with varying wollastonite (Wo; 32-44%), enstatite (En; 37-56%) and ferrosilite (Fs; 11-19%) components (Fig. 3). They are augites according to the nomenclature of Morimoto (1988) (Fig. 3) with low Cr₂O₃ contents (≤ 0.2 wt%; Table 1). They show similar compositions to the clinopyroxene megacrysts reported in Sun et al. (2020) (Figs. 3-5), which are from Xiadai, Mingxi, Yangyuan, Damaping, Dalinor and Jiucaidi (Fig. 1; Supplementary Table 6). They show varying Mg[#] ($= \text{Mg}/[\text{Mg} + \text{Fe}^{2+}]$) of 65-85 that correlates positively with SiO₂ and Cr₂O₃ contents and negatively with TiO₂, Al₂O₃, CaO and Na₂O contents (Fig. 4). In addition, these clinopyroxene megacrysts are compositionally distinct from the clinopyroxenes in mantle peridotite and pyroxenite xenoliths from eastern China but are similar to clinopyroxene megacrysts in worldwide alkali basalts (Fig. 4).

With decreasing Mg[#], incompatible trace element (e.g., Sr, La and Zr) abundances in these megacrysts increase (Figs. 5a-c), whereas Ni (491-8 $\mu\text{g/g}$) and Cu (6.83-1.24 $\mu\text{g/g}$) abundances decrease (Figs. 5d & e). Besides, these clinopyroxene megacrysts show large variations of [Sm/Yb]_N (subscript N denotes primitive mantle normalized

according to values in [Sun and McDonough \(1989\)](#)) (2.3-10.8) and Fe/Mn (38.8-77.0) that correlates negatively with $Mg^{\#}$ (also MgO) and Lu/Hf (0.01-0.16) and Sc/La (6.2-42.1) that correlates positively with $Mg^{\#}$ ([Figs. 5f-i](#)). They also show correlated variations of Yb with MnO, Sc and Y contents ([Figs. 5j-l](#)).

Sulphides

Most of the sulphide globules in the clinopyroxene megacrysts show within-grain compositional homogeneity ([Figs. 6a-c](#)). However, a few sulphide globules show heterogeneous distribution of Fe and Ni, with Ni concentrating at the edge of the sulphide globule ([Figs. 6d-f](#)). These sulphide globules are quantitatively insignificant, whose heterogeneous texture may result from low-temperature subsolidus breakdown or sulphide quenching during rapid ascent of host magmas ([Sen et al., 2010](#)). Different sulphide globules in the same clinopyroxene megacryst show relatively homogenous compositions (Supplementary Table 3). In the following discussion, we use average composition of sulphides in each clinopyroxene megacryst ([Table 2](#)).

These sulphides are Fe-Ni monosulphide solid solutions with S ranging from 37.55 to 40.89 wt %, Fe ranging from 52.86 to 59.04 wt %, Ni ranging from 0.50 to 7.78 wt %, low Cu (< 0.8 wt %) and Co (\leq 0.4 wt %) contents and minimal As, Pb and Zn ([Table 2](#)), which are similar to sulphides in Hawaiian garnet pyroxenite xenoliths ([Sen et al., 2010](#)) ([Fig. 7a](#)). A negative correlation exists between Ni and Fe contents in sulphides from different clinopyroxene megacrysts ([Fig. 7b](#)). Nickel contents in sulphides decrease with decreasing $Mg^{\#}$ of their host clinopyroxene megacrysts ([Fig.](#)

8). Clinopyroxene megacrysts from Jiucadi and Xiadai show similar relationships to those from the other locations, but with covariations that plot at lower values than the general trend (Fig. 8).

Host basalts

Major and trace element compositions of host basalts are given in Table 3, and those of clinopyroxene megacryst-bearing basalts reported in Sun et al. (2020), which are from Xiadai, Jiucadi, Mingxi, Yangyuan and Damaping, are given in Supplementary Table 7 and discussed together with the new data of this study. These basalts have $Mg^{\#}$ ranging from 44.0 to 65.3 and mostly in the small range of 56-60 (Fig. 9a), indicating variable extents of fractional crystallization from the expected primary magma of $Mg^{\#} \geq 72$ in equilibrium with mantle olivine of $Fo \geq \sim 90$ (Roeder & Emslie, 1970). They show scattered yet significant positive correlations of $Mg^{\#}$ (and MgO) with CaO (and CaO/Al₂O₃), MnO, Sc, Cr, Ni, Cu and heavy rare earth element (e.g., Lu) contents and negative correlations of $Mg^{\#}$ with [Sm/Yb]_N (4.2-11.6) and Fe/Mn (55-92) (Fig. 10).

DISCUSSION

Petrogenesis of clinopyroxene megacrysts

The correlated variations of $Mg^{\#}$ with major and trace elements in the clinopyroxene megacrysts (Figs. 4 & 5) and their compositional distinction from clinopyroxenes in mantle peridotite and pyroxenite xenoliths (Fig. 4) suggest that these

clinopyroxene megacrysts were crystallized from variably evolved parental magmas, rather than originating as fragments from mantle peridotite or pyroxenite wall-rocks. The within-grain homogeneous compositions suggest stable crystallizing conditions and maintained melt compositions.

However, these clinopyroxene megacrysts are not in chemical equilibrium with their host basalts ($Mg^{\#} = 44.0-65.3$) but had parental melts with more evolved $Mg^{\#}$ of 34.6-60.3 (Fig. 9b), calculated using a Fe-Mg exchange partition coefficient ($Kd_{\text{clinopyroxene-melt}}^{\text{Fe-Mg}}$) of 0.28 (Putirka, 2008). This is more apparent in the box and whisker plots (Fig. 9c) which show systematically lower $Mg^{\#}$ of melts in equilibrium with the clinopyroxene megacrysts from each location of eastern China than $Mg^{\#}$ of their host basalts. Therefore, these clinopyroxene megacrysts are xenocrysts captured during transport and eruption of their host basalts (Zhi et al., 1990; Tatsumoto et al., 1992; Sun et al., 2020). This is consistent with the inference that host magmas must ascend too fast to provide a stable environment to crystallize these megacrysts (Sun et al., 2018). Nevertheless, because melts parental to these clinopyroxene megacrysts have enriched incompatible element compositions that resemble those of the host basalts (Fig. 11), the host and parental melts of these clinopyroxene megacrysts must be derived from a common mantle source under similar conditions.

***P-T* conditions of crystallization**

Because these clinopyroxene megacrysts are not in chemical equilibrium with their host basalts, the single-clinopyroxene thermobarometer in Putirka (2008) (eq. 32a

and eq. 32d for pressure and temperature estimation with standard errors of estimate of ± 3.1 kbar and $\pm 58^\circ\text{C}$, respectively) was used to estimate the pressure (P) and temperature (T) conditions of crystallization. The calculated P - T results are given in Table 1 and plotted in Fig. 12 together with the P - T values of clinopyroxene megacrysts reported in Sun et al. (2020) (Supplementary Table 6). These clinopyroxene megacrysts were crystallized at 1240-1390°C and 18-30 kbar, corresponding to a depth range of ~60-95 km, calculated using an equation D (km) = $3.04 \times P$ (kbar) + 5.35 generated by estimating crust and lithospheric mantle densities beneath eastern China (Sun et al., 2018). Because the partitioning of Na between clinopyroxene and silicate melts is sensitive to pressure ($Kd_{\text{clinopyroxene} - \text{melt}}^{\text{Na}} \propto P$; Blundy et al., 1995; Putirka et al., 1996; Wood & Blundy, 2003; Bédard, 2014), with similar $\text{Mg}^\#$, clinopyroxene crystallized at higher pressures has higher Na contents. In the Na_2O - $\text{Mg}^\#$ diagram (Fig. 13), the studied clinopyroxene megacrysts plot in the overlapping field of clinopyroxenes experimentally crystallized at 20-30 kbar and 30-40 kbar, which confirms their high crystallization pressures. In the P - T diagram (Fig. 12), the calculated P - T values plot closely below the 1350°C mantle adiabat, between conductive geotherms of 65 mW/m^2 and 95 mW/m^2 and between the solidus and liquidus of alkali olivine basalts determined by experiment petrology (Green & Ringwood, 1967). The 60-95 km crystallization depths resemble the 60-100 km lithosphere-asthenosphere boundary (LAB) depths beneath eastern China (Chen et al., 2008; Li et al., 2013), and the conductive geotherms of 65-95 mW/m^2 are consistent with the present surface heat flow values of eastern

continental China (Hu et al., 2000; He, 2015). These observations are consistent with the crystallization of these clinopyroxene megacrysts at depths close to the LAB (Sun et al., 2020).

Because high-pressure fractional crystallization of basaltic magmas must have happened before mantle xenolith incorporation, the deepest equilibrium depth of mantle xenoliths from a given location gives a lower limit for the depth of fractional crystallization. To test this hypothesis, we compiled the equilibrium pressures (depths) of garnet peridotite and pyroxenite xenoliths (Xu et al., 1998; Qi et al., 1995; Lin et al., 1999; Huang & Xu, 2010) co-existing with the clinopyroxene megacrysts, which were calculated using a consistent set of geobarometers (Nickel & Green, 1985; Brey & Köhler, 1990). Mantle xenoliths from each location show a range of equilibrium pressures, suggesting they were captured from different depths (Fig. 14). Importantly, the depth of the deepest mantle xenoliths coincides within uncertainty with the seismically inferred LAB depth beneath each of these localities (Fig. 14). This agreement, although not precise because of the uncertainties associated with both geobarometry and seismic models, further substantiates that fractional crystallization of basaltic magmas happened before xenolith entrainment at depths close to the LAB.

Co-precipitation of clinopyroxene and garnet accompanied by immiscible separation of sulphide melts

The increasing $[\text{Sm}/\text{Yb}]_{\text{N}}$ and Fe/Mn and decreasing Lu/Hf and Sc/La with decreasing $\text{Mg}^{\#}$ in the clinopyroxene megacrysts (Figs. 5f-i) reflect large compositional

variations of their parental melts during crystallization (Figs. 15a-c). These compositional changes of the parental melts cannot be explained by crystallization of clinopyroxene megacrysts alone, but also require garnet to be co-precipitated with clinopyroxene because Mn, Sc and heavy rare earth elements (e.g., Yb, Lu and Y) are highly compatible in garnet (Irving & Frey, 1978; Zack et al., 1997; Adam & Green, 2006). This is corroborated by the positive correlations of Yb with MnO, Sc and Y contents in these clinopyroxene megacrysts (Figs. 5j-l). Geochemical modelling using $[Sm/Yb]_N$, Fe/Mn and Sc/La requires co-precipitation of ~ 80% clinopyroxene and 20% garnet to explain the data (Figs. 15d & e), which is consistent with the abundant clinopyroxene and lesser garnet megacrysts in these basalts. The rarity of garnet megacryst may also result from transport inhibition due to its high density and more rounded shape.

The decreasing Ni with decreasing $Mg^\#$ in the clinopyroxene megacrysts (Fig. 5d) reflects a large decrease of Ni (from ~ 152 to 3 $\mu\text{g/g}$) in their parental melts (Fig. 15f) during crystallization. Such large Ni variation cannot be adequately explained by fractional crystallization of clinopyroxene which has only a moderate partition coefficient for Ni ($Kd_{\text{Clinopyroxene} - \text{Melt}}^{\text{Ni}} = \sim 3$; Le Roux et al., 2011). Decreasing melt Ni content with decreasing $Mg^\#$ is usually explained by fractional crystallization of olivine. However, experimental studies on alkali basalts demonstrate the absence of olivine on the liquidus during precipitation of garnet and clinopyroxene at high pressures, with olivine becoming a liquidus phase at lower pressures (e.g., < 18 kbar;

Bultitude & Green, 1967; Green & Ringwood, 1967; O'Hara & Yoder, 1967). Olivine grains in alkali basalts of eastern China mostly have high Fo values and low CaO contents; thus, they represent xenocrysts from peridotite xenoliths (Zhi et al., 1990; Dostal et al., 1991; Sakuyama et al., 2013; Sun et al., 2017). In addition, $Kd_{Ol-melt}^{Ni}$ values decrease with increasing pressure, with olivines crystallized at high pressures having lower $Kd_{Ol-melt}^{Ni}$ values (e.g., $Kd_{Ol-melt}^{Ni}$ [3 GPa] = ~ 2.0; Niu et al., 2011). Even if olivines co-precipitated with clinopyroxene megacrysts at high pressures, their effect on melt Ni content would be insignificant compared with that at low pressures. Therefore, the varying Ni contents in the clinopyroxene megacrysts and their parental melts cannot be explained by fractional crystallization of olivine.

The clinopyroxene megacrysts show decreasing Cu concentrations with decreasing Mg[#] (Fig. 5e) and a Ni-Cu covariation in their parental melts (Fig. 15f). This Ni-Cu covariation cannot be explained by fractional crystallization of olivine, clinopyroxene and garnet, but can be explained by immiscible separation of sulphides from basaltic melts (Fig. 15f), because sulphides have high partition coefficients for both Ni and Cu (e.g., $Kd_{sulphide\ melt - silicate\ melt}^{Ni} = 776$ and $Kd_{sulphide\ melt - silicate\ melt}^{Cu} = 1334$; Pattern et al., 2013). This is consistent with the abundant sulphide globules in the clinopyroxene megacrysts (Figs. 2e & f). The observed covariation between sulphide Ni contents and host clinopyroxene Mg[#] (Fig. 8) suggests the sulphide globules and host clinopyroxene megacrysts are in chemical equilibrium and co-genetic. Therefore,

we conclude that the clinopyroxene and garnet megacrysts crystallized concurrently with immiscibility between sulphide and basaltic melts.

The abundant sulphide inclusions in the clinopyroxene megacrysts are consistent with a high-pressure origin. Basaltic melts are inferred to be sulphide-saturated when extracted from the mantle with immiscible sulphide droplets entrained in the segregating silicate melts (Keays, 1995; Mavrogenes & O'Neill, 1999). However, during melt ascent, decompression results in a sharp increase of the sulfur content at sulphide saturation which causes silicate melts to become sulphide-undersaturated and to dissolve immiscible sulphide melts (Mavrogenes & O'Neill, 1999; Bockrath et al., 2004; Liu et al., 2007; Wallace et al., 2015). Sulphide saturation of basaltic magmas at low pressures could be achieved after substantial fractional crystallization (Mavrogenes & O'Neill, 1999). However, the abundant mantle xenoliths and clinopyroxene and garnet megacrysts in the Cenozoic basalts in eastern China indicate limited low-pressure fractional crystallization during their ascent. Therefore, the dense immiscible sulphide droplets in the clinopyroxene megacrysts were most likely fractionated from basaltic melts at conditions near the asthenospheric mantle source region or close beneath the LAB. This is consistent with the inference that the LAB is a zone with Cu and platinum group elements enrichment because of sulphide segregation (Lorand et al., 1993). Spherical sulphide inclusions in clinopyroxenes of the garnet pyroxenite xenoliths from the Salt Lake Crater, Hawaii, which show compositional similarity to

sulphides in the clinopyroxene megacrysts of this study (Fig. 7a), were explained in a similar manner (Sen et al., 2010).

Because segregation of immiscible sulphide melts can deplete Ni in the silicate melts so strongly, Ni depletion in basaltic magmas cannot be used indiscriminately as an indicator of fractional crystallization of olivine, as earlier suggested by Andersen et al. (1987). Importantly, although the olivine addition method has been used to infer the primary compositions of oceanic tholeiitic basalts (e.g., Putirka, 2005; Herzberg, 2006; Lee et al., 2009; Gale et al., 2014), caution is needed when applying this method to alkali basalts. This is because clinopyroxene and garnet, *not* olivine, are early liquidus phases at high pressures relevant to intra-plate basaltic magmatism and the effect of their fractional crystallization on melt compositional variations must be considered when constructing primitive magmas to infer mantle potential temperatures.

Influence of high-pressure fractional crystallization on basalt compositions

The compositional variations of clinopyroxene megacryst-bearing basalts (Fig. 10) are consistent with their having experienced variable extents of fractional crystallization of clinopyroxene and garnet and immiscible fractionation of sulphides. Therefore, these basalts and their included clinopyroxene megacrysts, although not in chemical equilibrium with each other, should be products of the same magmatic system. The variably low Mg[#], CaO (Fig. 10a) and MnO (Fig. 10b) contents and high [Sm/Yb]_N (Fig. 10h) and Fe/Mn (Fig. 10i) in these basalts result from fractional crystallization of clinopyroxene and garnet, rather than indicate a garnet pyroxenite mantle source with

low $Mg^\#$ (e.g., subducted oceanic crust) as suggested in previous studies (Liu et al., 2008a; Yang & Zhou, 2013; Yang et al., 2016). Although mantle pyroxenites have been suggested as sources of oceanic alkali basalts (e.g., Sobolev et al., 2005, 2007; Hirschmann & Stolper, 1996), melts from pyroxenites will still achieve chemical equilibrium with ambient mantle peridotite to have $Mg^\# \geq 72$, because of the low volume of pyroxenites in the mantle (Niu, 2016). Therefore, low basalt $Mg^\#$ must reflect compositional evolution by fractional crystallization. These basalts (Fig. 10i) and melts in equilibrium with clinopyroxene megacrysts (Fig. 15a) with highest $Mg^\#$ have Fe/Mn ~ 60 which is indistinguishable from Fe/Mn of global mantle peridotites (Fe/Mn = 60 ± 10 ; McDonough & Sun, 1995) and that of primitive ($Mg^\# \geq 68$) MORB glasses (Fe/Mn = 57 ± 11 , n = 298) (MORB data were from the PetDB Database, www.earthchem.org/petdb) but is lower than Fe/Mn (> 60 ; Liu et al., 2008) of pyroxenite-derived melts. Therefore, Cenozoic basalts in eastern China are more likely to have been derived from a peridotite, instead of a pyroxenite mantle source, which is also the case for intraplate ocean island basalts (Niu et al., 2011; Niu, 2018).

Existence of sulphide-rich melts ponded under the LAB

The significant correlations of $Mg^\#$ with major and trace elements and their ratios in the clinopyroxene megacrysts (Figs. 4 & 5) suggest that the clinopyroxene megacrysts, although coming from different locations, were crystallized from melts with similar primitive compositions (Fig. 15) and thus similar mantle sources and melting conditions. Melts in equilibrium with the clinopyroxene megacrysts have low

[Sm/Yb]_N (~ 4.0) at Mg[#] = 60 (Fig. 15a), and even lower [Sm/Yb]_N values are expected for more primitive melts. Basalt [Sm/Yb]_N has been a reliable indicator of the pressure of melt-solid equilibration in the mantle. Melts extracted at high pressures in the garnet peridotite facies experience low degrees of decompression melting with a prominent “garnet signature” (high Sm/Yb). Such “garnet signature” would be diluted by increasing extents of decompression melting with melts extracted at low pressures having low Sm/Yb (Ellam, 1992; Haase, 1996; Niu et al., 2011; Davies et al., 2015; Guo et al., 2020; Sun et al., 2020). Therefore, the primitive melts parental to the clinopyroxene megacrysts show similarly “low” pressures of melt-solid equilibration. Because the base of the lithosphere limits the final depths of melt extraction or equilibration in the mantle (Niu et al., 2011; Guo et al., 2020; Sun et al., 2020), the primitive melts parental to the clinopyroxene megacrysts most likely all have experienced low-pressure equilibration near the LAB. Therefore, large volumes of melts ponded under the LAB are expected, which is consistent with crystallization of compositionally uniform clinopyroxene megacrysts and segregation of immiscible sulphides from these melts at the LAB depths.

A melt-rich layer beneath the suboceanic LAB has been inferred from the petrology and geochemistry of ocean island basalts (Niu & O’Hara, 2009; Niu & Green, 2018) and detected seismically (Kawakatsu et al., 2009; Sifré et al., 2014; Naif et al., 2013), which may form by accumulation of incipient melts from deeper in the asthenosphere (Green, 2015; Niu & Green, 2018). The upper mantle beneath eastern

China shows low seismic velocity at ~ 100-150 km that resembles the seismic structure of the upper mantle beneath young ocean basins (Ekström & Dziewonski, 1998), which also requires a melt-rich layer present beneath the LAB (Fig. 16a) (Chen et al., 2006; Niu, 2014; Sun et al., 2021). Melt pools in this melt-rich layer (Fig. 16b) can provide a stable and closed environment for crystallizing clinopyroxene and garnet megacrysts (Sun et al., 2020). Studies of garnet pyroxenite xenoliths in ocean island basalts indicate high-pressure accumulation in melt pools atop the asthenosphere (e.g., Sen & Jones, 1990; Keshav et al., 2007). Crystallization of clinopyroxene and garnet will decrease Mg[#], CaO, MnO and heavy rare earth element contents and increase [Sm/Yb]_N and Fe/Mn in the residual melts, which can be conveniently misinterpreted as being derived from a garnet-pyroxenite mantle source. Segregation of minor immiscible sulphide melts would cause Ni and Cu depletion in the silicate melts. Subsequent pulses of melt aggregation from upwelling mantle columns with more primitive compositions can disturb these melt pools, cause magma mixing and trigger the eruption of magmas carrying clinopyroxene and garnet megacrysts (Fig. 16c). Therefore, we suggest that high-pressure crystallization in the melt-rich layer close beneath the LAB is significant for understanding the petrological and geochemical characteristics of Cenozoic basalts in eastern China and elsewhere in continental settings as well as “Petit spots” type melts erupted on mature ocean floors (Hirano et al., 2006).

CONCLUSIONS

- (1) The geochemical variations of clinopyroxene megacrysts in the Cenozoic basalts in eastern China are consistent with crystallization from variably evolved melts. Their parental melts are more evolved than the host basalts, indicating these clinopyroxene megacrysts were xenocrysts. Their equilibrium P - T conditions (18-30 kbar and 1240-1390 °C) are close to those of the LAB beneath eastern China.
- (2) The correlated variations of $Mg^{\#}$ with $[Sm/Yb]_N$, Lu/Hf, Sc/La and Fe/Mn in the clinopyroxene megacrysts are consistent with their co-precipitation with garnet. Geochemical modelling suggests co-precipitation of ~ 80% clinopyroxene and 20% garnet.
- (3) The decreasing Cu and Ni contents with decreasing $Mg^{\#}$ in the clinopyroxene megacrysts indicate immiscibility between sulphide and silicate melts concurrent with the growth of clinopyroxene megacrysts, which is consistent with abundant sulphide globules in the clinopyroxene megacrysts. An observed covariation of Ni contents in the sulphide globules with $Mg^{\#}$ of the host clinopyroxene megacrysts proves that the sulphides and clinopyroxene megacrysts are co-genetic. The abundant sulphide globules in the clinopyroxene megacrysts are consistent with a high-pressure origin.
- (4) Because the segregation of immiscible sulphide melts can strongly deplete Ni in the silicate melts, Ni depletion in basaltic magmas cannot be used indiscriminately as an indicator of fractional crystallization of olivine. In addition, caution is needed

when applying the olivine addition method to infer the primary compositions of alkali basalts. This is because unlike tholeiitic basalts in which olivine appears early on the liquidus, alkali basalts with a high-pressure origin should have clinopyroxene and garnet as early liquidus phases.

- (5) High-pressure crystallization of clinopyroxene and garnet, instead of their residence in the mantle source, resulted in high Fe/Mn and $[\text{Sm}/\text{Yb}]_N$ in the host basalts with low and variable $\text{Mg}^\#$. Primitive host basalts and melts in equilibrium with the clinopyroxene megacrysts have Fe/Mn indistinguishable from mantle peridotite and primitive MORB glasses, suggesting a peridotite, instead of a pyroxenite mantle source. Caution is required when using parameters of basalt CaO and MnO contents, Fe/Mn and Sm/Yb to infer mantle source lithologies without considering the effects of high-pressure crystallization of clinopyroxene and garnet.
- (6) The primitive melts parental to the clinopyroxene megacrysts show low $[\text{Sm}/\text{Yb}]_N$ (~ 4.0), suggesting their final equilibration at low pressures close to the LAB. Therefore, a melt-rich layer close beneath the LAB is required. This melt-rich layer is accumulated by incipient melts from deeper asthenosphere. Melt pools in this melt-rich layer provide a stable environment to crystallize clinopyroxene megacrysts with uniform compositions. As a result, melts in these melt pools are variably evolved with low $\text{Mg}^\#$. Subsequent pulses of melt aggregation from depths with primitive compositions and high $\text{Mg}^\#$ will disturb these melt layers, cause

magma mixing and trigger the eruption of magmas that carry clinopyroxene and garnet megacrysts and deep-seated mantle xenoliths.

ACKNOWLEDGEMENTS

We thank Dr. Hilary Downes, Dr. Emily J. Chin and two anonymous reviewers for their careful reviews and constructive comments. We thank Dr. Jason Harvey for his editorial work and useful suggestions. Dr. Zhiqing Lai is thanked for assistance during electron microprobe analysis. This study was supported by grants from the Shandong Provincial Natural Science Foundation (ZR2020MD029), National Natural Science Foundation of China (NSFC) (41630968, 42006049), NSFC-Shandong Joint Fund for Marine Science Research Centers (U1606401), the Qingdao National Laboratory for Marine Science and Technology (2015ASKJ03) and 111 Project (B18048).

REFERENCE

- Adam, J. & Green, T. (2006). Trace element partitioning between mica- and amphibole-bearing garnet lherzolite and hydrous basanitic melt: 1. Experimental results and the investigation of controls on partitioning behaviour. *Contributions to Mineralogy and Petrology* **152**, 1-17.
- Akinin, V. V., Sobolev, A. V., Ntaflos, T. & Richter, W. (2005). Clinopyroxene megacrysts from Enmelen melanephelinitic volcanoes (Chukchi Peninsula,

- Russia): application to composition and evolution of mantle melts. *Contributions to Mineralogy and Petrology* **150**, 85-101.
- Andersen, T., Griffin, W. L. & O'Reilly, S. Y. (1987). Primary sulphide melt inclusions in mantle-derived megacrysts and pyroxenites. *Lithos* **20**, 279-294.
- Bédard, J. H. (2014). Parameterizations of calcic clinopyroxene—Melt trace element partition coefficients. *Geochemistry, Geophysics, Geosystems* **15**, 303-336.
- Bézos, A., Lorand, J. P., Humler, E. & Gros, M. (2005). Platinum-group element systematics in Mid-Oceanic Ridge basaltic glasses from the Pacific, Atlantic, and Indian Oceans. *Geochimica et Cosmochimica Acta* **69**, 2613-2627.
- Bizimis, M., Sen, G., Salters, V. J. M. & Keshav, S. (2005). Hf-Nd-Sr isotope systematics of garnet pyroxenites from Salt Lake Crater, Oahu, Hawaii: Evidence for a depleted component in Hawaiian volcanism. *Geochimica et Cosmochimica Acta* **69**, 2629-2646.
- Blundy, J., Falloon, T., Wood, B. & Dalton, J. (1995). Sodium partitioning between clinopyroxene and silicate melts. *Journal of Geophysical Research: Solid Earth (1978–2012)* **100**, 15501-15515.
- Bockrath, C., Ballhaus, C. & Holzheid, A. (2004). Fractionation of the Platinum-Group Elements During Mantle Melting. *Science* **305**, 1951.
- Brey, G. P. & Köhler, T. (1990). Geothermobarometry in Four-phase Lherzolites II. New Thermobarometers, and Practical Assessment of Existing Thermobarometers. *Journal of Petrology* **31**, 1353-1378.

- Bultitude, R. J. & Green, D. H. (1967). Experimental study at high pressures on the origin of olivine nephelinite and olivine melilite nephelinite magmas. *Earth and Planetary Science Letters* **3**, 325-337.
- Chen, L. (2009). Lithospheric structure variations between the eastern and central North China Craton from S- and P-receiver function migration. *Physics of the Earth and Planetary Interiors* **173**, 216-227.
- Chen, L., Tao, W., Zhao, L. & Zheng, T. (2008). Distinct lateral variation of lithospheric thickness in the Northeastern North China Craton. *Earth and Planetary Science Letters* **267**, 56-68.
- Chen, L., Zheng, T. & Xu, W. (2006). A thinned lithospheric image of the Tanlu Fault Zone, eastern China: Constructed from wave equation based receiver function migration. *Journal of Geophysical Research: Solid Earth* **111**, B09312.
- Chen, S., Wang, X., Niu, Y., Sun, P., Duan, M., Xiao, Y., Guo, P., Gong, H., Wang, G. & Xue, Q. (2017). Simple and cost-effective methods for precise analysis of trace element abundances in geological materials with ICP-MS. *Science Bulletin* **62**, 277-289.
- Czamanske, G. K. & Moore, J. G. (1977). Composition and phase chemistry of sulfide globules in basalt from the Mid-Atlantic Ridge rift valley near 37°N lat. *GSA Bulletin* **88**, 587-599.

- Davies, D. R., Rawlinson, N., Iaffaldano, G. & Campbell, I. H. (2015). Lithospheric controls on magma composition along Earth's longest continental hotspot track. *Nature* **525**, 511-514.
- Dobosi, G. & Jenner, G. (1999). Petrologic implications of trace element variation in clinopyroxene megacrysts from the Nograd volcanic province, north Hungary: a study by laser ablation microprobe-inductively coupled plasma-mass spectrometry. *Lithos* **46**, 731-749.
- Dostal, J., Zhi, X., Muehlenbachs, K., Dupuy, C. & Zhai, M. (1991). Geochemistry of Cenozoic alkali basaltic lavas from Shandong Province, eastern China. *Geochemical Journal* **25**, 1-16.
- Ekström, G. & Dziewonski, A. M. (1998). The unique anisotropy of the Pacific upper mantle. *Nature* **394**, 168-172.
- Ellam, R. M. (1992). Lithospheric thickness as a control on basalt geochemistry. *Geology* **20**, 153-156.
- Frey, F. A. (1980). The origin of pyroxenites and garnet pyroxenites from Salt Lake crater, Oahu, Hawaii: Trace element evidence. *American Journal of Science* **280**, 427-449.
- Gale, A., Langmuir, C. H. & Dalton, C. A. (2014). The Global Systematics of Ocean Ridge Basalts and their Origin. *Journal of Petrology* **55**, 1051-1082.
- Green, D. H. (1966). The origin of the "eclogites" from Salt Lake Crater, Hawaii. *Earth and Planetary Science Letters* **1**, 414-420.

- Green, D. H. (2015). Experimental petrology of peridotites, including effects of water and carbon on melting in the Earth's upper mantle. *Physics and Chemistry of Minerals* **42**, 95-122.
- Green, D. H., Edgar, A. D., Beasley, P., Kiss, E. & Ware, N. G. (1974). Upper mantle source for some hawaiites, mugearites and benmoreites. *Contributions to Mineralogy and Petrology* **48**, 33-43.
- Green, D. H. & Ringwood, A. E. (1964). Fractionation of Basalt Magmas at High Pressures. *Nature* **201**, 1276.
- Green, D. H. & Ringwood, A. E. (1967). The genesis of basaltic magmas. *Contributions to Mineralogy and Petrology* **15**, 103-190.
- Guo, P., Niu, Y., Sun, P., Zhang, J., Chen, S., Duan, M., Gong, H. & Wang, X. (2021). The nature and origin of upper mantle heterogeneity beneath the Mid-Atlantic Ridge 33–35°N: A Sr-Nd-Hf isotopic perspective. *Geochimica et Cosmochimica Acta* **307**, 72-85.
- Haase, K. M. (1996). The relationship between the age of the lithosphere and the composition of oceanic magmas: Constraints on partial melting, mantle sources and the thermal structure of the plates. *Earth and Planetary Science Letters* **144**, 75-92.
- Harvey, J., Warren, J. M. & Shirey, S. B. (2016). Mantle Sulfides and their Role in Re-Os and Pb Isotope Geochronology. *Reviews in Mineralogy and Geochemistry* **81**, 579-649.

- He, L. (2015). Thermal regime of the North China Craton: Implications for craton destruction. *Earth-Science Reviews* **140**, 14-26.
- Herzberg, C. (2006). Petrology and thermal structure of the Hawaiian plume from Mauna Kea volcano. *Nature* **444**, 605.
- Hirano, N., Takahashi, E., Yamamoto, J., Abe, N., Ingle, S. P., Kaneoka, I., Hirata, T., Kimura, J.-I., Ishii, T., Ogawa, Y., Machida, S. & Suyehiro, K. (2006). Volcanism in Response to Plate Flexure. *Science* **313**, 1426.
- Hirschmann, M. M. & Stolper, E. M. (1996). A possible role for garnet pyroxenite in the origin of the “garnet signature” in MORB. *Contributions to Mineralogy and Petrology* **124**, 185-208.
- Hole, M. J. (2018). Mineralogical and geochemical evidence for polybaric fractional crystallization of continental flood basalts and implications for identification of peridotite and pyroxenite source lithologies. *Earth-Science Reviews* **176**, 51-67.
- Hu, S., He, L. & Wang, J. (2000). Heat flow in the continental area of China: a new data set. *Earth and Planetary Science Letters* **179**, 407-419.
- Huang, X. & Xu, Y. (2010). Thermal state and structure of the lithosphere beneath eastern China: A synthesis on basalt-borne xenoliths. *Journal of Earth Science* **21**, 711-730.
- Humayun, M., Qin, L. & Norman, M. D. (2004). Geochemical Evidence for Excess Iron in the Mantle Beneath Hawaii. *Science* **306**, 91.

- Irving, A. J. & Frey, F. A. (1978). Distribution of trace elements between garnet megacrysts and host volcanic liquids of kimberlitic to rhyolitic composition. *Geochimica et Cosmochimica Acta* **42**, 771-787.
- Irving, A. J. & Green, D. H. (2008). Phase Relationships of Hydrous Alkalic Magmas at High Pressures: Production of Nepheline Hawaiitic to Mugearitic Liquids by Amphibole-Dominated Fractional Crystallization Within the Lithospheric Mantle. *Journal of Petrology* **49**, 741-756.
- Irving, A. J. & Price, R. C. (1981). Geochemistry and evolution of Iherzolite-bearing phonolitic lavas from Nigeria, Australia, East Germany and New Zealand. *Geochimica et Cosmochimica Acta* **45**, 1309-1320.
- Kawakatsu, H., Kumar, P., Takei, Y., Shinohara, M., Kanazawa, T., Araki, E. & Suyehiro, K. (2009). Seismic Evidence for Sharp Lithosphere-Asthenosphere Boundaries of Oceanic Plates. *Science* **324**, 499-502.
- Keays, R. R. (1995). The role of komatiitic and picritic magmatism and S-saturation in the formation of ore deposits. *Lithos* **34**, 1-18.
- Keshav, S., Sen, G. & Presnall, D. C. (2007). Garnet-bearing Xenoliths from Salt Lake Crater, Oahu, Hawaii: High-Pressure Fractional Crystallization in the Oceanic Mantle. *Journal of Petrology* **48**, 1681-1724.
- Kullerud, G., Yund, R.A., Moh, G.H. (1969). Phase relations in the Cu-Fe-S, Cu-Ni-S, and Fe-Ni-S systems. *Economic Geology Monograph* **4**, 323-343.

- Lai, Z., Zhao, G., Han, Z., Huang, B., Li, M., Tian, L., Liu, B. & Bu, X. (2018). The magma plumbing system in the Mariana Trough back-arc basin at 18° N. *Journal of Marine Systems* **180**, 132-139.
- Le Roux, V., Dasgupta, R. & Lee, C. T. A. (2011). Mineralogical heterogeneities in the Earth's mantle: Constraints from Mn, Co, Ni and Zn partitioning during partial melting. *Earth and Planetary Science Letters* **307**, 395-408.
- Lee, C.-T. A., Luffi, P., Chin, E. J., Bouchet, R., Dasgupta, R., Morton, D. M., Le Roux, V., Yin, Q.-z. & Jin, D. (2012). Copper Systematics in Arc Magmas and Implications for Crust-Mantle Differentiation. *Science* **336**, 64-68.
- Lee, C.-T. A., Luffi, P., Plank, T., Dalton, H. & Leeman, W. P. (2009). Constraints on the depths and temperatures of basaltic magma generation on Earth and other terrestrial planets using new thermobarometers for mafic magmas. *Earth and Planetary Science Letters* **279**, 20-33.
- Li, H.-Y., Xu, Y.-G., Ryan, J. G., Huang, X.-L., Ren, Z.-Y., Guo, H. & Ning, Z.-G. (2016). Olivine and melt inclusion chemical constraints on the source of intracontinental basalts from the eastern North China Craton: Discrimination of contributions from the subducted Pacific slab. *Geochimica et Cosmochimica Acta* **178**, 1-19.
- Li, Y.-Q., Ma, C.-Q., Robinson, P. T., Zhou, Q. & Liu, M.-L. (2015). Recycling of oceanic crust from a stagnant slab in the mantle transition zone: Evidence from

- Cenozoic continental basalts in Zhejiang Province, SE China. *Lithos* **230**, 146-165.
- Li, Y., Wu, Q., Pan, J., Zhang, F. & Yu, D. (2013). An upper-mantle S-wave velocity model for East Asia from Rayleigh wave tomography. *Earth and Planetary Science Letters* **377-378**, 367-377.
- Lin, C., Shi, L., Chen, X. & Han, X. (1999). Thermal structure and rheology of the upper mantle beneath Mingxi, Fujian Province. *Geological Review* **45**, 352-360.
- Liu, C.-Q., Masuda, A. & Xie, G.-H. (1992). Isotope and trace-element geochemistry of alkali basalts and associated megacrysts from the Huangyishan volcano, Kuandian, Liaoning, NE China. *Chemical Geology* **97**, 219-231.
- Liu, Y., Gao, S., Kelemen, P. B. & Xu, W. (2008a). Recycled crust controls contrasting source compositions of Mesozoic and Cenozoic basalts in the North China Craton. *Geochimica et Cosmochimica Acta* **72**, 2349-2376.
- Liu, Y., Hu, Z., Gao, S., Günther, D., Xu, J., Gao, C. & Chen, H. (2008b). In situ analysis of major and trace elements of anhydrous minerals by LA-ICP-MS without applying an internal standard. *Chemical Geology* **257**, 34-43.
- Liu, Y., Samaha, N.-T. & Baker, D. R. (2007). Sulfur concentration at sulfide saturation (SCSS) in magmatic silicate melts. *Geochimica et Cosmochimica Acta* **71**, 1783-1799.
- Lorand, J. P., Keays, R. R. & Bodinier, J. L. (1993). Copper and Noble Metal Enrichments Across the Lithosphere—Asthenosphere Boundary of Mantle

- Diapirs: Evidence from the Lanzo Lherzolite Massif. *Journal of Petrology* **34**, 1111-1140.
- Mavrogenes, J. A. & O'Neill, H. S. C. (1999). The relative effects of pressure, temperature and oxygen fugacity on the solubility of sulfide in mafic magmas. *Geochimica et Cosmochimica Acta* **63**, 1173-1180.
- McDonough, W. F. & Sun, S. s. (1995). The composition of the Earth. *Chemical Geology* **120**, 223-253.
- Morimoto, N. (1988). Nomenclature of Pyroxenes. *Mineralogy and Petrology* **39**, 55-76.
- Naif, S., Key, K., Constable, S. & Evans, R. L. (2013). Melt-rich channel observed at the lithosphere–asthenosphere boundary. *Nature* **495**, 356-359.
- Nickel, K. G. & Green, D. H. (1985). Empirical geothermobarometry for garnet peridotites and implications for the nature of the lithosphere, kimberlites and diamonds. *Earth and Planetary Science Letters* **73**, 158-170.
- Niu, Y. (2014). Geological understanding of plate tectonics: basic concepts, illustrations, examples and new perspectives. *Global Tectonics and Metallogeny*. **10**, 23-46.
- Niu, Y. (2016). The Meaning of Global Ocean Ridge Basalt Major Element Compositions. *Journal of Petrology* **57**, 2081-2103.

- Niu, Y. (2018). Origin of the LLSVPs at the base of the mantle is a consequence of plate tectonics – A petrological and geochemical perspective. *Geoscience Frontiers* **9**, 1265-1278.
- Niu, Y. & Green, D. H. (2018). The petrological control on the lithosphere-asthenosphere boundary (LAB) beneath ocean basins. *Earth-Science Reviews* **185**, 301-307.
- Niu, Y. & O'Hara, M. J. (2009). MORB mantle hosts the missing Eu (Sr, Nb, Ta and Ti) in the continental crust: new perspectives on crustal growth, crust–mantle differentiation and chemical structure of oceanic upper mantle. *Lithos* **112**, 1-17.
- Niu, Y. & O'Hara, M. J. (2008). Global correlations of ocean ridge basalt chemistry with axial depth: a new perspective. *Journal of Petrology* **49**, 633-664.
- Niu, Y., Wilson, M., Humphreys, E. R. & O'Hara, M. J. (2011). The origin of intra-plate ocean island basalts (OIB): the lid effect and its geodynamic implications. *Journal of Petrology* **52**, 1443-1468.
- O'Hara, M. J. (1968). The bearing of phase equilibria studies in synthetic and natural systems on the origin and evolution of basic and ultrabasic rocks. *Earth-Science Reviews* **4**, 69-133.
- O'Hara, M. J., Saunders, M. J. & Mercy, E. L. P. (1975). 39 - GARNET-PERIDOTITE, PRIMARY ULTRABASIC MAGMA AND ECLOGITE; INTERPRETATION OF UPPER MANTLE PROCESSES IN KIMBERLITE. In: Ahrens, L. H.,

- Dawson, J. B., Duncan, A. R. & Erlank, A. J. (eds.) *Physics and Chemistry of the Earth*: Pergamon, 571-604.
- O'Hara, M. J. (1965). Primary magmas and the origin of basalts. *Scottish Journal of Geology* **1**, 19-40.
- O'Hara, M. J. & Yoder, H. S. (1967). Formation and fractionation of basic magmas at high pressures. *Scottish Journal of Geology* **3**, 67-117.
- Pang, C.-J., Wang, X.-C., Li, C.-F., Wilde, S. A. & Tian, L. (2019). Pyroxenite-derived Cenozoic basaltic magmatism in central Inner Mongolia, eastern China: Potential contributions from the subduction of the Paleo-Pacific and Paleo-Asian oceanic slabs in the Mantle Transition Zone. *Lithos* **332-333**, 39-54.
- Patten, C., Barnes, S.-J., Mathez, E. A. & Jenner, F. E. (2013). Partition coefficients of chalcophile elements between sulfide and silicate melts and the early crystallization history of sulfide liquid: LA-ICP-MS analysis of MORB sulfide droplets. *Chemical Geology* **358**, 170-188.
- Peterson, R. & Francis, D. (1977). The origin of sulfide inclusions in pyroxene megacrysts. *American Mineralogist* **62**, 1049-1051.
- Pollack, H. N. & Chapman, D. S. (1977). On the regional variation of heat flow, geotherms, and lithospheric thickness. *Tectonophysics* **38**, 279-296.
- Price, R. C. & Green, D. H. (1972). Lherzolite Nodules in a "Mafic Phonolite" from North-east Otago, New Zealand. *Nature Physical Science* **235**, 133-134.

- Putirka, K., Johnson, M., Kinzler, R., Longhi, J. & Walker, D. (1996). Thermobarometry of mafic igneous rocks based on clinopyroxene-liquid equilibria, 0–30 kbar. *Contributions to Mineralogy and Petrology* **123**, 92-108.
- Putirka, K. D. (2005). Mantle potential temperatures at Hawaii, Iceland, and the mid-ocean ridge system, as inferred from olivine phenocrysts: Evidence for thermally driven mantle plumes. *Geochemistry, Geophysics, Geosystems* **6**, Q05L08.
- Putirka, K. D. (2008). Thermometers and barometers for volcanic systems. *Reviews in Mineralogy and Geochemistry* **69**, 61-120.
- Qi, Q., Taylor, L. A. & Zhou, X. (1995). Petrology and Geochemistry of Mantle Peridotite Xenoliths from SE China. *Journal of Petrology* **36**, 55-79.
- Rankenburg, K., Lassiter, J. C. & Brey, G. (2004). Origin of megacrysts in volcanic rocks of the Cameroon volcanic chain – constraints on magma genesis and crustal contamination. *Contributions to Mineralogy and Petrology* **147**, 129-144.
- Roeder, P. & Emslie, R. (1970). Olivine-liquid equilibrium. *Contributions to Mineralogy and Petrology* **29**, 275-289.
- Sakuyama, T., Tian, W., Kimura, J.-I., Fukao, Y., Hirahara, Y., Takahashi, T., Senda, R., Chang, Q., Miyazaki, T., Obayashi, M., Kawabata, H. & Tatsumi, Y. (2013). Melting of dehydrated oceanic crust from the stagnant slab and of the hydrated mantle transition zone: Constraints from Cenozoic alkaline basalts in eastern China. *Chemical Geology* **359**, 32-48.

- Sen, G. (1988). Petrogenesis of spinel lherzolite and pyroxenite suite xenoliths from the Koolau shield, Oahu, Hawaii: Implications for petrology of the post-eruptive lithosphere beneath Oahu. *Contributions to Mineralogy and Petrology* **100**, 61-91.
- Sen, G. & Jones, R. E. (1990). Cumulate Xenolith in Oahu, Hawaii: Implications for Deep Magma Chambers and Hawaiian Volcanism. *Science* **249**, 1154.
- Sen, I. S., Bizimis, M. & Sen, G. (2010). Geochemistry of sulfides in Hawaiian garnet pyroxenite xenoliths: Implications for highly siderophile elements in the oceanic mantle. *Chemical Geology* **273**, 180-192.
- Shan, B., Xiong, X., Zhao, K. F., Xie, Z. J., Zheng, Y. & Zhou, L. (2016). Crustal and upper-mantle structure of South China from Rayleigh wave tomography. *Geophysical Journal International* **208**, 1643-1654.
- Shaw, C. S. & Eyzaguirre, J. (2000). Origin of megacrysts in the mafic alkaline lavas of the West Eifel volcanic field, Germany. *Lithos* **50**, 75-95.
- Sifré, D., Gardés, E., Massuyeau, M., Hashim, L., Hier-Majumder, S. & Gaillard, F. (2014). Electrical conductivity during incipient melting in the oceanic low-velocity zone. *Nature* **509**, 81-85.
- Sobolev, A. V., Hofmann, A. W., Kuzmin, D. V., Yaxley, G. M., Arndt, N. T., Chung, S.-L., Danyushevsky, L. V., Elliott, T., Frey, F. A., Garcia, M. O., Gurenko, A. A., Kamenetsky, V. S., Kerr, A. C., Krivolutsкая, N. A., Matvienkov, V. V., Nikogosian, I. K., Rocholl, A., Sigurdsson, I. A., Sushchevskaya, N. M. & Teklay,

- M. (2007). The Amount of Recycled Crust in Sources of Mantle-Derived Melts. *Science* **316**, 412-417.
- Sobolev, A. V., Hofmann, A. W., Sobolev, S. V. & Nikogosian, I. K. (2005). An olivine-free mantle source of Hawaiian shield basalts. *Nature* **434**, 590-597.
- Sun, P., Guo, P. & Niu, Y. (2021). Eastern China continental lithosphere thinning is a consequence of paleo-Pacific plate subduction: A review and new perspectives. *Earth-Science Reviews*, 103680.
- Sun, P., Niu, Y., Guo, P., Cui, H., Ye, L. & Liu, J. (2018). The evolution and ascent paths of mantle xenolith-bearing magma: Observations and insights from Cenozoic basalts in Southeast China. *Lithos* **310–311**, 171-181.
- Sun, P., Niu, Y., Guo, P., Duan, M., Wang, X., Gong, H. & Xiao, Y. (2020). The Lithospheric Thickness Control on the Compositional Variation of Continental Intraplate Basalts: A Demonstration Using the Cenozoic Basalts and Clinopyroxene Megacrysts From Eastern China. *Journal of Geophysical Research: Solid Earth* **125**, e2019JB019315.
- Sun, P., Niu, Y., Guo, P., Ye, L., Liu, J. & Feng, Y. (2017). Elemental and Sr–Nd–Pb isotope geochemistry of the Cenozoic basalts in Southeast China: Insights into their mantle sources and melting processes. *Lithos* **272–273**, 16-30.
- Sun, S.-S. & McDonough, W. (1989). Chemical and isotopic systematics of oceanic basalts: implications for mantle composition and processes. *Geological Society, London, Special Publications* **42**, 313-345.

- Tatsumoto, M., Basu, A. R., Wankang, H., Junwen, W. & Guanghong, X. (1992). Sr, Nd, and Pb isotopes of ultramafic xenoliths in volcanic rocks of Eastern China: enriched components EMI and EMII in subcontinental lithosphere. *Earth and Planetary Science Letters* **113**, 107-128.
- Wallace, P. J., Plank, T., Edmonds, M. & Hauri, E. H. (2015). Chapter 7 - Volatiles in Magmas. In: Sigurdsson, H. (ed.) *The Encyclopedia of Volcanoes (Second Edition)*. Amsterdam: Academic Press, 163-183.
- Wang, X.-C., Wilde, S. A., Li, Q.-L. & Yang, Y.-N. (2015). Continental flood basalts derived from the hydrous mantle transition zone. *Nature Communications* **6**, 7700.
- Wang, Y., Zhao, Z.-F., Zheng, Y.-F. & Zhang, J.-J. (2011). Geochemical constraints on the nature of mantle source for Cenozoic continental basalts in east-central China. *Lithos* **125**, 940-955.
- Wood, B. J. & Blundy, J. (2003). Trace element partitioning under crustal and uppermost mantle conditions: the influence of ionic radius, cation charge, pressure, and temperature. *Treatise on Geochemistry* **2**, 395-423.
- Woodland, A. & Jugo, P. (2007). A complex magmatic system beneath the Deves volcanic field, Massif Central, France: evidence from clinopyroxene megacrysts. *Contributions to Mineralogy and Petrology* **153**, 719-731.
- Wright, J. B. (1966). Olivine Nodules in a Phonolite of the East Otago Alkaline Province, New Zealand. *Nature* **210**, 519-519.

- Xiao, Y., Chen, S., Niu, Y., Wang, X., Xue, Q., Wang, G., Gao, Y., Gong, H., Kong, J., Shao, F., Sun, P., Duan, M., Hong, D. & Wang, D. (2020). Mineral Compositions of Syn-collisional Granitoids and their Implications for the Formation of Juvenile Continental Crust and Adakitic Magmatism. *Journal of Petrology* **61**, egaa038.
- Xu, X., O'Reilly, S. Y., Griffin, W. L., Zhou, X. & Huang, X. (1998). The Nature of the Cenozoic Lithosphere at Nushan, Eastern China. *Mantle dynamics and plate interactions in East Asia*: American Geophysical Union, 167-195.
- Yang, A. Y., Zhou, M.-F., Zhao, T.-P., Deng, X.-G., Qi, L. & Xu, J.-F. (2014). Chalcophile elemental compositions of MORBs from the ultraslow-spreading Southwest Indian Ridge and controls of lithospheric structure on S-saturated differentiation. *Chemical Geology* **382**, 1-13.
- Yang, Z.-F., Li, J., Liang, W.-F. & Luo, Z.-H. (2016). On the chemical markers of pyroxenite contributions in continental basalts in Eastern China: Implications for source lithology and the origin of basalts. *Earth-Science Reviews* **157**, 18-31.
- Yang, Z.-F. & Zhou, J.-H. (2013). Can we identify source lithology of basalt? *Scientific reports* **3**, 1856.
- Yoder, J. H. S. & Tilley, C. E. (1962). Origin of Basalt Magmas: An Experimental Study of Natural and Synthetic Rock Systems. *Journal of Petrology* **3**, 342-532.

- Yu, X., Zeng, G., Chen, L.-H., Hu, S.-L. & Yu, Z.-Q. (2019). Magma–magma interaction in the mantle recorded by megacrysts from Cenozoic basalts in eastern China. *International Geology Review* **61**, 675-691.
- Yu, X., Zeng, G., Chen, L.-H., Wang, X.-J., Liu, J., Xie, L. & Yang, T. (2018). Evidence for rutile-bearing eclogite in the mantle sources of the Cenozoic Zhejiang basalts, eastern China. *Lithos* **324**.
- Zack, T., Foley, S. F. & Jenner, G. A. (1997). A consistent partition coefficient set for clinopyroxene, amphibole and garnet from laser ablation microprobe analysis of garnet pyroxenites from Kakanui, New Zealand. *Neues Jahrbuch für Mineralogie-Abhandlungen* **172**, 23-41.
- Zeng, G., Chen, L.-H., Hu, S.-L., Xu, X.-S. & Yang, L.-F. (2013). Genesis of Cenozoic low-Ca alkaline basalts in the Nanjing basaltic field, eastern China: The case for mantle xenolith-magma interaction. *Geochemistry, Geophysics, Geosystems* **14**, 1660-1677.
- Zhang, B., Liu, Y. & Gao, S. (2008). Petrogenetic significance of high Fe/Mn ratios of the Cenozoic basalts from eastern China. *Science in China Series D: Earth Sciences* **51**, 229-239.
- Zhang, J.-J., Zheng, Y.-F. & Zhao, Z.-F. (2009). Geochemical evidence for interaction between oceanic crust and lithospheric mantle in the origin of Cenozoic continental basalts in east-central China. *Lithos* **110**, 305-326.

Zhi, X., Song, Y., Frey, F. A., Feng, J. & Zhai, M. (1990). Geochemistry of Hannuoba basalts, eastern China: Constraints on the origin of continental alkalic and tholeiitic basalt. *Chemical Geology* **88**, 1-33.

FIGURE CAPTIONS

Figure 1 Spatial distribution of Cenozoic volcanism in eastern continental China and sample localities. Modified from [Sun et al. \(2017\)](#).

Figure 2 Hand specimens of clinopyroxene (Cpx) (a & c) and garnet (b & c) megacrysts, cross-polarized light (XPL) photomicrographs of clinopyroxene megacrysts (d-e) with abundant sulphide globules (opaque spots) (e) and photomicrograph of these sulphide globules under reflected light (f).

Figure 3 Wo (wollastonite)-En (Enstatite)-Fs (ferrosilite) composition of clinopyroxene megacrysts ([Morimoto, 1988](#)).

Figure 4 Plots of SiO₂, TiO₂, CaO, Al₂O₃, Na₂O and Cr₂O₃ against Mg[#] (= 100×Mg/Mg + Fe²⁺) in the clinopyroxene megacrysts from eastern China. For comparison, compositions of clinopyroxene megacrysts in worldwide alkali basalts ([Dobsi & Jenner, 1999](#); [Shaw & Eyzaguirre, 2000](#); [Rankenburg et al., 2004](#); [Akinin et al., 2005](#); [Woodland & Jugo, 2007](#)) and clinopyroxenes in mantle peridotite and pyroxenite xenoliths from eastern China (from GEOROC database: <http://georoc.mpch-mainz.gwdg.de/georoc/Start.asp>) are also plotted.

Figure 5 Plots of Sr, La, Zr, Ni, Cu, [Sm/Yb]_N, Lu/Hf, Sc/La and Fe/Mn against Mg[#] (a-i) and correlations of Yb with MnO, Sc and Y (j-l) in the clinopyroxene megacrysts.

Figure 6 Backscattered electron (BSE) images and chemical (Fe and Ni) maps of a compositionally homogeneous sulphide grain (a-c) and a compositionally heterogeneous sulphide grain (d-f) in the clinopyroxene megacrysts. Note that the slight variations of colors within the sulphide grain in (b) and (c) do not indicate compositional variations but are caused by interference of cracks in the sulphide grain on the signal intensities. The same portions in the sulphide grain being white in (d), green in (e) and red in (f) are Ni-rich.

Figure 7 (a) Sulphide compositions in the Fe–Ni–S system (Kullerud et al., 1969). For comparison, the compositions of sulphides in Hawaiian pyroxenites (Sen et al., 2010) are also plotted. (b) A negative correlation between Ni and Fe contents in sulphides from different clinopyroxene megacrysts. The error bars indicate one standard deviation (± 1 SD) from the mean.

Figure 8 Plots of Ni contents in the sulphides against Mg[#] of the host clinopyroxene megacrysts. Each data point represents average Ni contents in the sulphides from a given clinopyroxene megacryst (Y-axis) and average Mg[#] of this clinopyroxene megacryst (X-axis). The error bars indicate one standard deviation (± 1 SD) from the mean.

Figure 9 Histograms (a & b) and box and whisker plots (c) of $Mg^{\#}$ of clinopyroxene megacryst-bearing basalts and melts in equilibrium with the clinopyroxene megacrysts. The box in (c) spans the interquartile range. The horizontal line and the cross inside each box represent the median and average, respectively. The two lines extending from the box (the whiskers) indicate the highest and lowest values, respectively. The circles outside the box indicate outliers.

Figure 10 Plots of CaO, MnO, Sc, Cr, Ni, Cu, Lu, $[Sm/Yb]_N$ and Fe/Mn against $Mg^{\#}$ in the host basalts of clinopyroxene megacrysts.

Figure 11 Primitive mantle normalized multiple incompatible element abundances of melts in equilibrium with the clinopyroxene megacrysts and their host basalts from Kuandian, Dalinor, Penglai and Nanjing. Compositions of melts in equilibrium with the clinopyroxene megacrysts were calculated using the partition coefficients in [Zack et al. \(1997\)](#). Composition of primitive mantle is from [Sun & McDonough \(1989\)](#).

Figure 12 Plots of calculated pressures (P) and temperatures (T) of the clinopyroxene megacrysts. The mantle adiabat for mantle potential temperature (T_p) of 1350 °C, the liquidus and solidus of alkali olivine basalts ([Green & Ringwood, 1967](#)) and the continental conductive geotherms of 65 mW/m² and 95 mW/m² modelled using the method of [Pollack & Chapman \(1977\)](#) are also plotted.

Figure 13 Comparison between clinopyroxene megacrysts in eastern China and experimentally crystallized clinopyroxenes at various pressure ranges (shaded areas) in the Na₂O (wt %)-Mg[#] plot. The data plotted include those of clinopyroxene megacrysts reported in this study and those reported in [Sun et al. \(2020\)](#). The data of experimentally crystallized clinopyroxenes are from LEPR (Library of Experimental Phase Relations; <https://earthchem.org/data-access/>) database.

Figure 14 Comparison between the equilibrium pressures (depths) of garnet peridotite and pyroxenite xenoliths co-existing with clinopyroxene megacrysts and the seismically inferred lithosphere-asthenosphere boundary (LAB) depths beneath eastern China. The equilibrium pressures of garnet peridotite and pyroxenite xenoliths include those compiled in [Huang & Xu \(2010\)](#) and those we compiled from the literature ([Xu et al., 1998](#); [Qi et al., 1995](#); [Lin et al., 1998](#)). These pressure values were calculated using the geothermobarometers of [Nickel & Green \(1985\)](#) and [Brey & Köhler \(1990\)](#), which were demonstrated to be reliable for garnet-facies xenoliths ([Xu et al., 1998](#)). The equilibrium pressures of spinel-facies xenoliths were not compiled because there is no reliable geobarometer for these rocks. The depth values were calculated using an empirical equation: $D \text{ (km)} = 3.04 \text{ (km/kbar)} \times P \text{ (kbar)} + 5.35 \text{ (km)}$ ([Sun et al., 2018](#)), which was generated by estimating the crust (32 km) and lithospheric mantle densities of eastern China. The LAB depths beneath different regions of eastern China were approximated from seismic studies ([Chen et al., 2008](#); [Chen, 2009](#); [Li et al., 2013](#); [Shan et al., 2016](#)).

Figure 15 Plots of $Mg^{\#}$ with $[Sm/Yb]_N$ (a), Fe/Mn (b) and Sc/La (c) of melts in equilibrium with the clinopyroxene megacrysts. The effects of fractional crystallization of clinopyroxene, garnet and olivine on melt compositions are modelled in the plots of $[Sm/Yb]_N$ with Sc/La (d) and Fe/Mn (e). The parental melt with lowest $[Sm/Yb]_N$ was approximated as the primitive melt. The effect of immiscible fractionation of sulphide is modelled in the Cu-Ni plot (f) with the parental melt having both highest Cu and Ni as the primitive melt. The partition coefficients of Sm, Yb, Sc and La for clinopyroxene and garnet are from [Zack et al. \(1997\)](#), and those for olivine are from [Adam & Green \(2006\)](#). The partition coefficients of Ni and Cu for clinopyroxene and garnet are from [Lee et al. \(2012\)](#), and those for sulphide are from [Pattern et al. \(2013\)](#). The partition coefficients of Fe and Mn for clinopyroxene, garnet and olivine are from [Liu et al. \(2008\)](#) with $Kd_{clinopyroxene - Melt}^{Fe/Mn}$ of 0.65.

Figure 16 Schematic illustrations for the generation and evolution of Cenozoic basalts in eastern China. Incipient melts that formed at depths (~ 80-250 km; [Green, 2015](#); [Sun et al., 2021](#)) migrate upwards because of their low density and accumulate at the LAB, forming a melt-rich layer with reduced seismic velocity ([Chen et al., 2006](#)) (a). This melt-rich layer was inferred to consist of horizontally aligned melt pools embedded in the meltless mantle matrix (e.g., [Kawakatsu et al., 2009](#)) (b). These melt pools can provide a stable environment for crystallizing compositionally uniform clinopyroxene and garnet megacrysts concurrent with immiscible fractionation and accumulation of sulphide melt globules (c). Therefore, melts in these melt pools are variably evolved

with low $Mg^{\#}$, low CaO and MnO contents and high Fe/Mn and $[Sm/Yb]_N$. Subsequent pulses of magma aggregation from upwelling mantle columns with more primitive compositions (higher $Mg^{\#}$) will disturb these melt pools, cause magma mixing and trigger the eruption of magmas carrying clinopyroxene and garnet megacrysts (c).

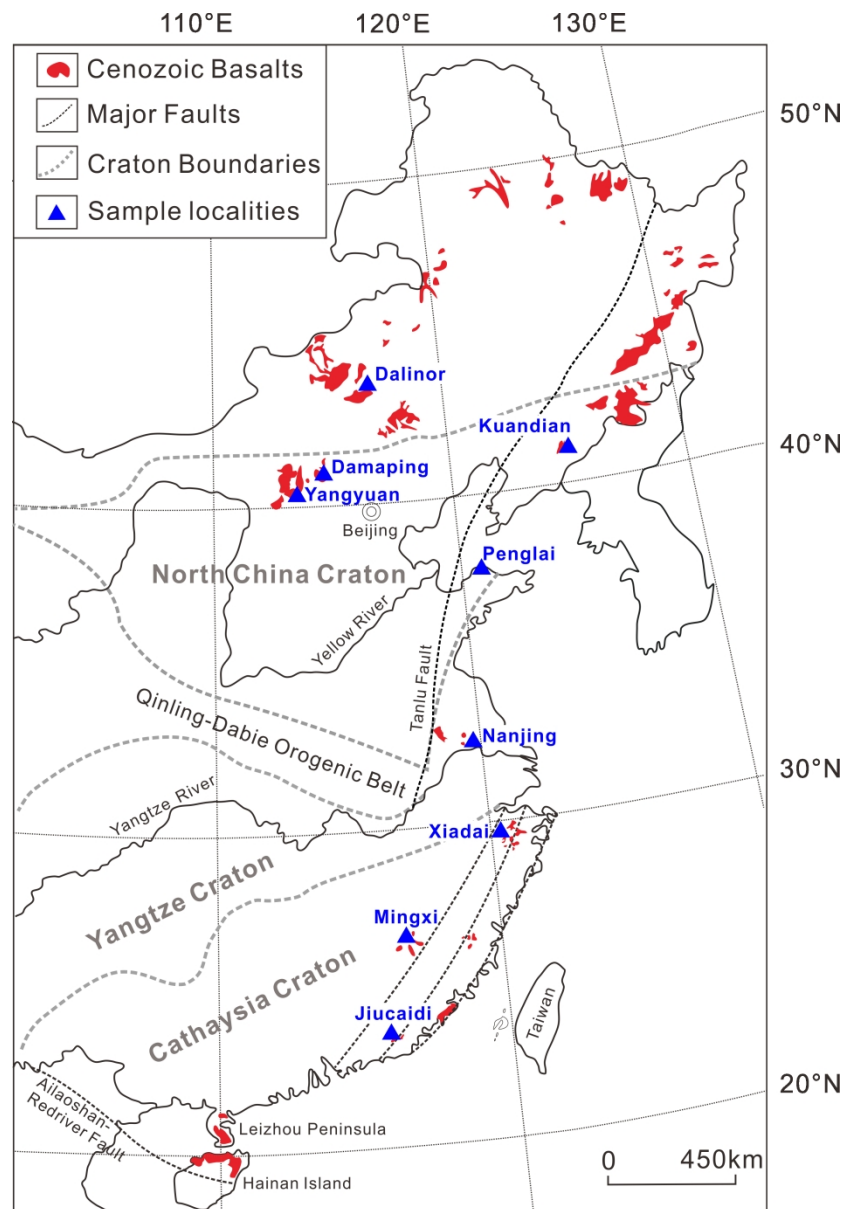


Figure 1 Spatial distribution of Cenozoic volcanism in eastern continental China and sample localities. Modified from Sun et al. (2017).

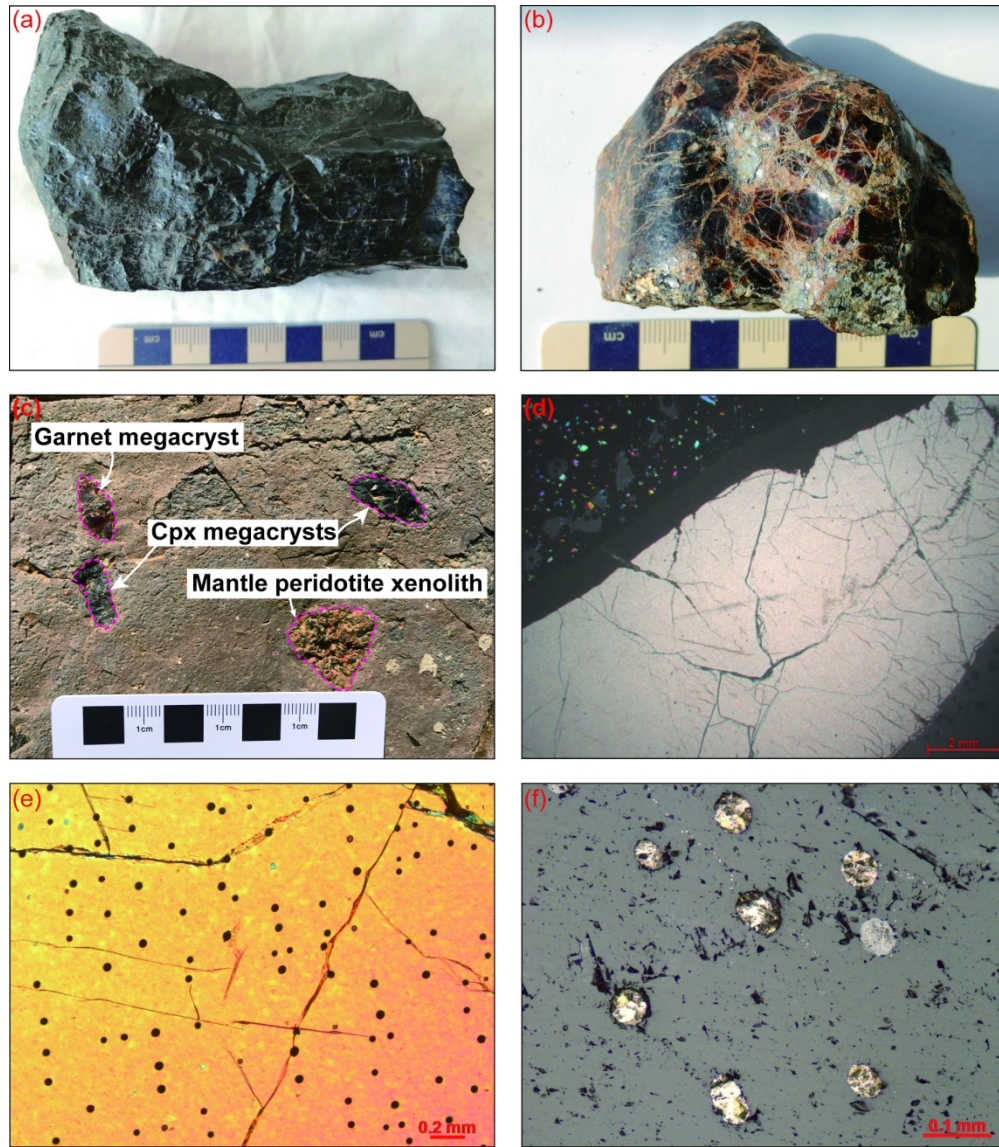


Figure 2 Hand specimens of clinopyroxene (Cpx) (a & c) and garnet (b & c) megacrysts, cross-polarized light (XPL) photomicrographs of clinopyroxene megacrysts (d-e) with abundant sulphide globules (opaque spots) (e) and photomicrograph of these sulphide globules under reflected light (f).

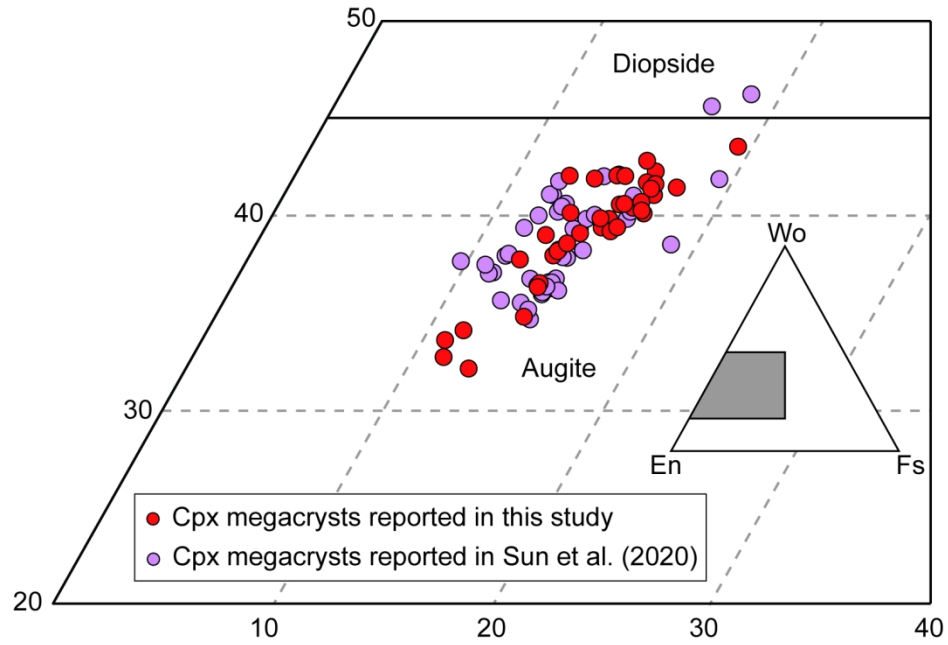


Figure 3 Wo (wollastonite)-En (Enstatite)-Fs (ferrosilite) composition of clinopyroxene megacrysts (Morimoto, 1988).

147x95mm (300 x 300 DPI)

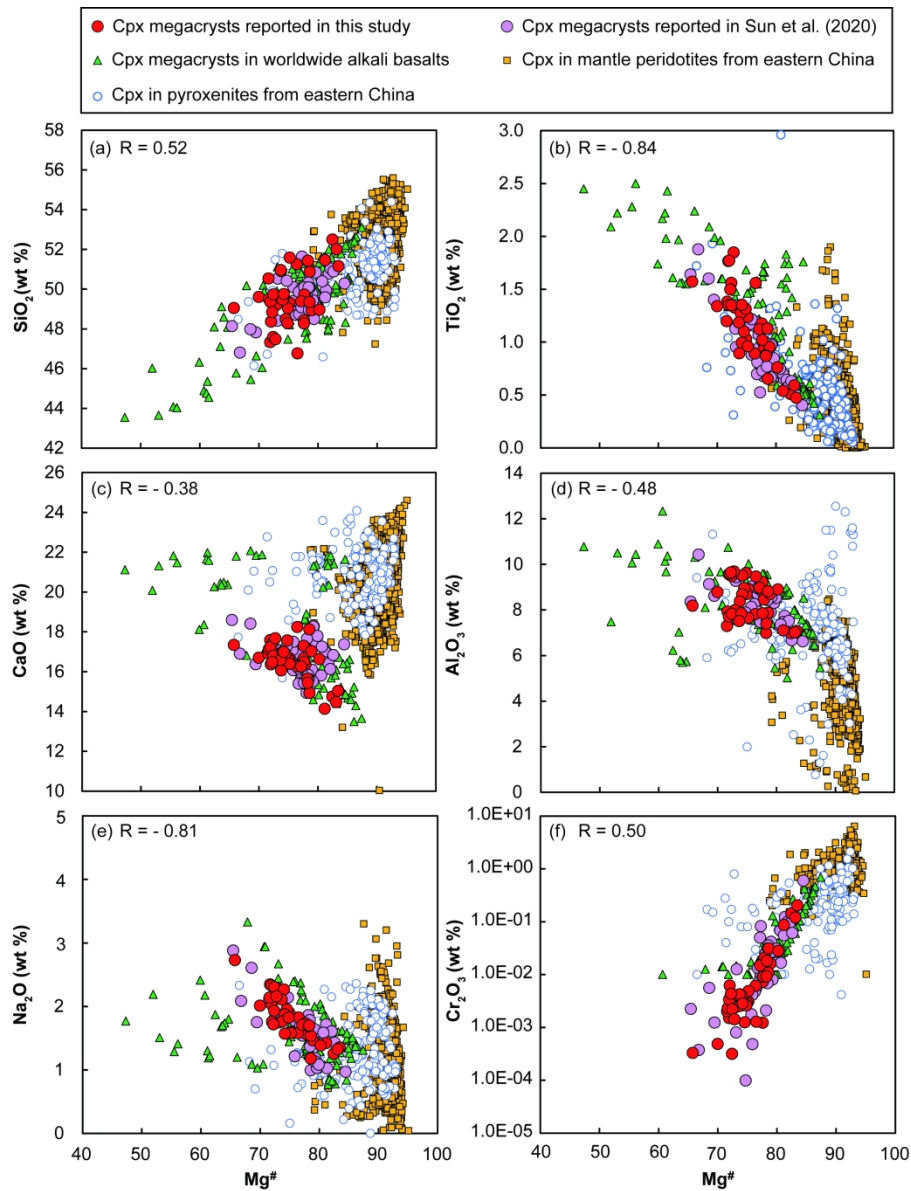


Figure 4 Plots of SiO₂, TiO₂, CaO, Al₂O₃, Na₂O and Cr₂O₃ against Mg# in the clinopyroxene megacrysts from eastern China. For comparison, compositions of clinopyroxene megacrysts in worldwide alkali basalts (Dobson and Jenner, 1999; Shaw and Eyzaguirre, 2000; Rankenburg et al., 2004; Akinin et al., 2005; Woodland and Jugo, 2007) and clinopyroxenes in mantle peridotite and pyroxenite xenoliths from eastern China (from GEOROC database: <http://georoc.mpch-mainz.gwdg.de/georoc/Start.asp>) are also plotted.

207x261mm (300 x 300 DPI)

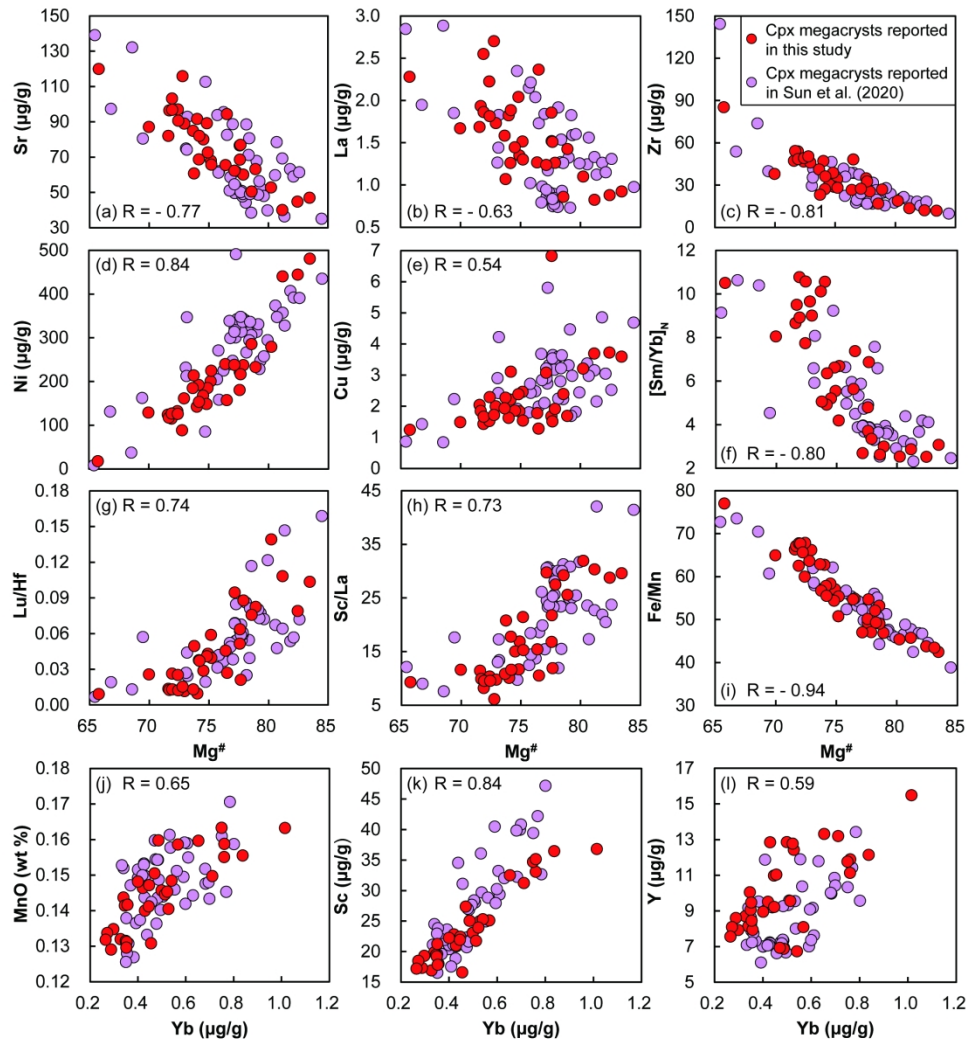


Figure 5 Plots of Sr, La, Zr, Ni, Cu, $[Sm/Yb]_N$, Lu/Hf, Sc/La and Fe/Mn against $Mg^\#$ (a-i) and correlations of Yb with MnO, Sc and Y (j-l) in the clinopyroxene megacrysts.

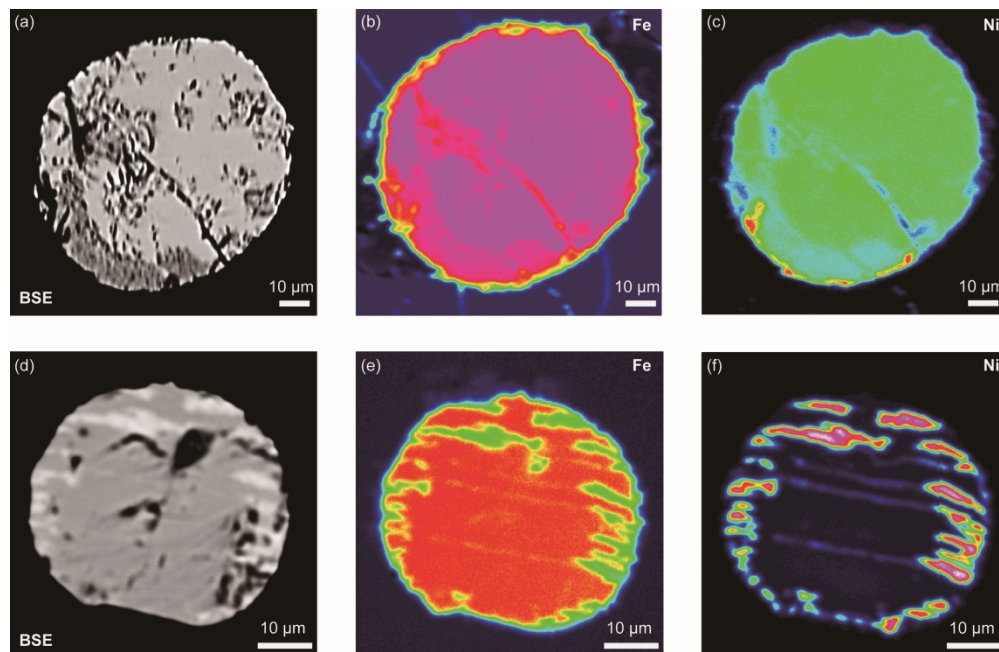


Figure 6 Backscattered electron (BSE) images and chemical (Fe and Ni) maps of a compositionally homogeneous sulphide grain (a-c) and a compositionally heterogeneous sulphide grain (d-f) in the clinopyroxene megacrysts. Note that the slight variations of colors within the sulphide grain in (b) and (c) do not indicate compositional variations but are caused by interference of cracks in the sulphide grain on the signal intensities. The same portions in the sulphide grain being white in (d), green in (e) and red in (f) are Ni-rich.

236x153mm (300 x 300 DPI)

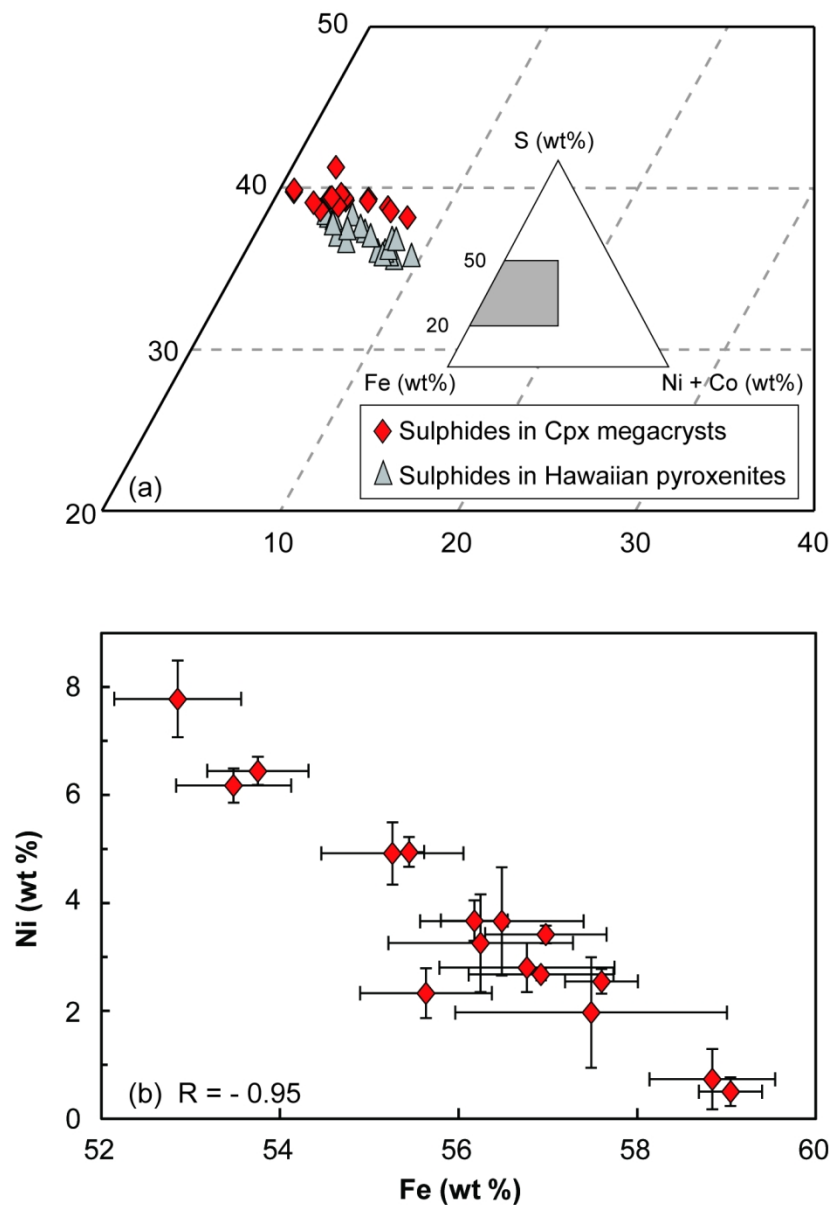


Figure 7 (a) Sulphide compositions in the Fe–Ni–S system (Kullerud et al., 1969). For comparison, the compositions of sulphides in Hawaiian pyroxenites (Sen et al., 2010) are also plotted. (b) A negative correlation between Ni and Fe contents in sulphides from different clinopyroxene megacrysts. The error bars indicate one standard deviation (± 1 SD) from the mean.

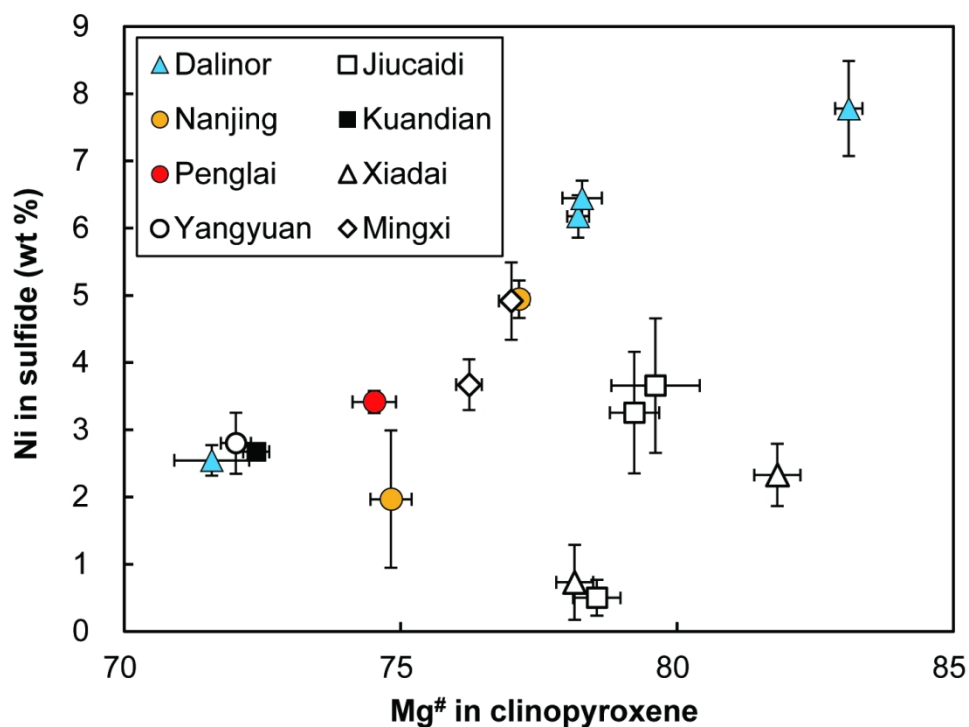


Figure 8 Plots of Ni contents in the sulphides against Mg[#] of the host clinopyroxene megacrysts. Each data point represents average Ni contents in the sulphides from a given clinopyroxene megacryst (Y-axis) and average Mg[#] of this clinopyroxene megacryst (X-axis). The error bars indicate one standard deviation (± 1 SD) from the mean.

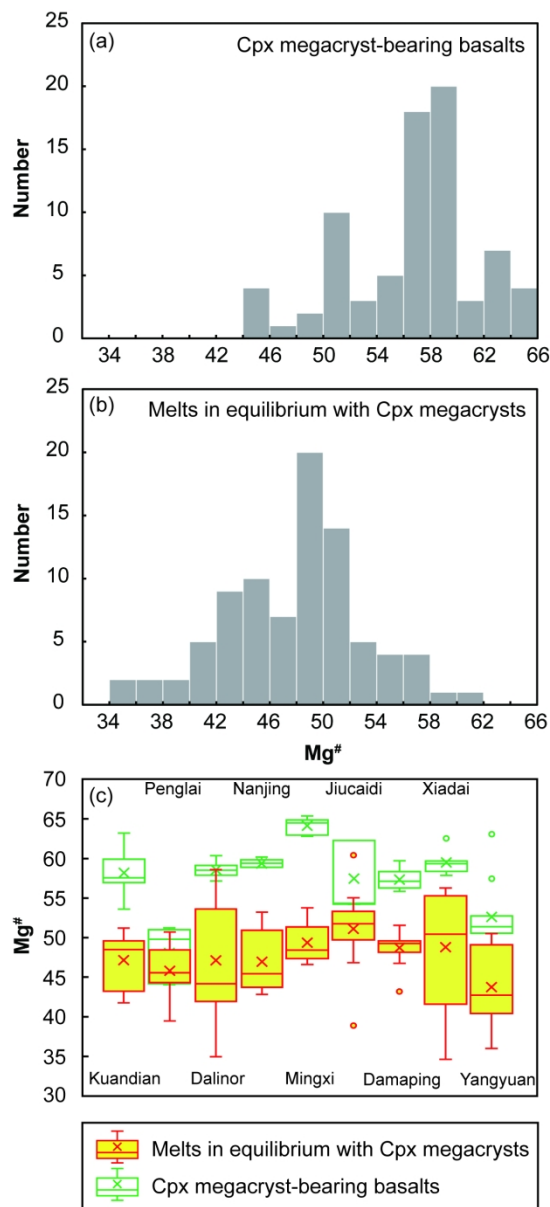


Figure 9 Histograms (a & b) and box and whisker plots (c) of Mg[#] of clinopyroxene megacryst-bearing basalts and melts in equilibrium with the clinopyroxene megacrysts. The box in (c) spans the interquartile range. The horizontal line and the cross inside each box represent the median and average, respectively. The two lines extending from the box (the whiskers) indicate the highest and lowest values, respectively. The circles outside the box indicate outliers.

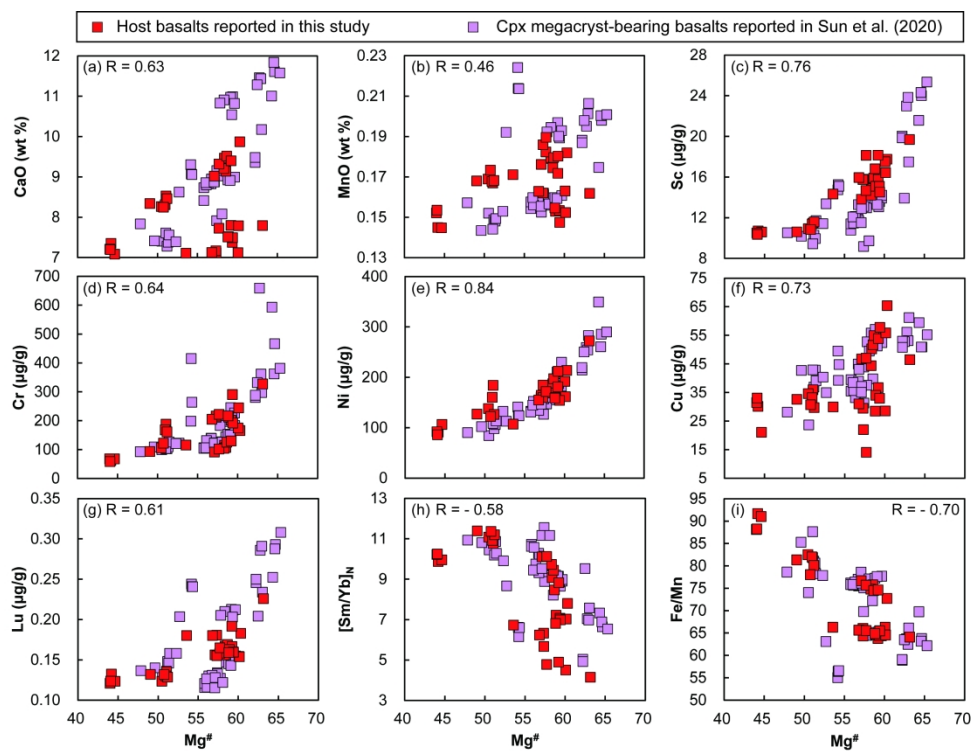


Figure 10 Plots of CaO, MnO, Sc, Cr, Ni, Cu, Lu, [Sm/Yb]_N and Fe/Mn against Mg[#] in the host basalts of clinopyroxene megacrysts.

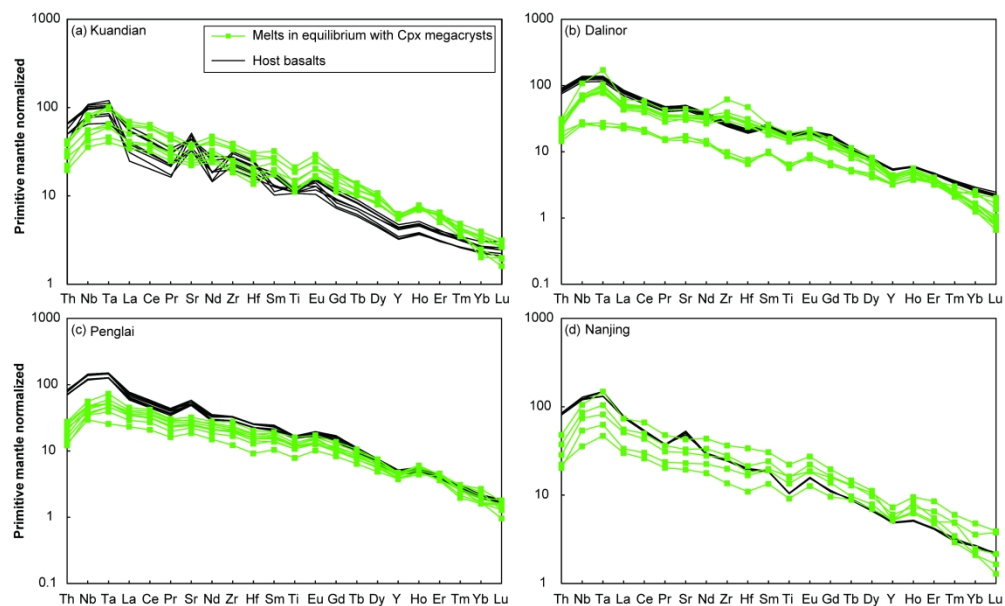


Figure 11 Primitive mantle normalized multiple incompatible element abundances of melts in equilibrium with the clinopyroxene megacrysts and their host basalts from Kuandian, Dalinor, Penglai and Nanjing. Compositions of melts in equilibrium with the clinopyroxene megacrysts were calculated using the partition coefficients in Zack et al. (1997). Composition of primitive mantle is from Sun and McDonough (1989).

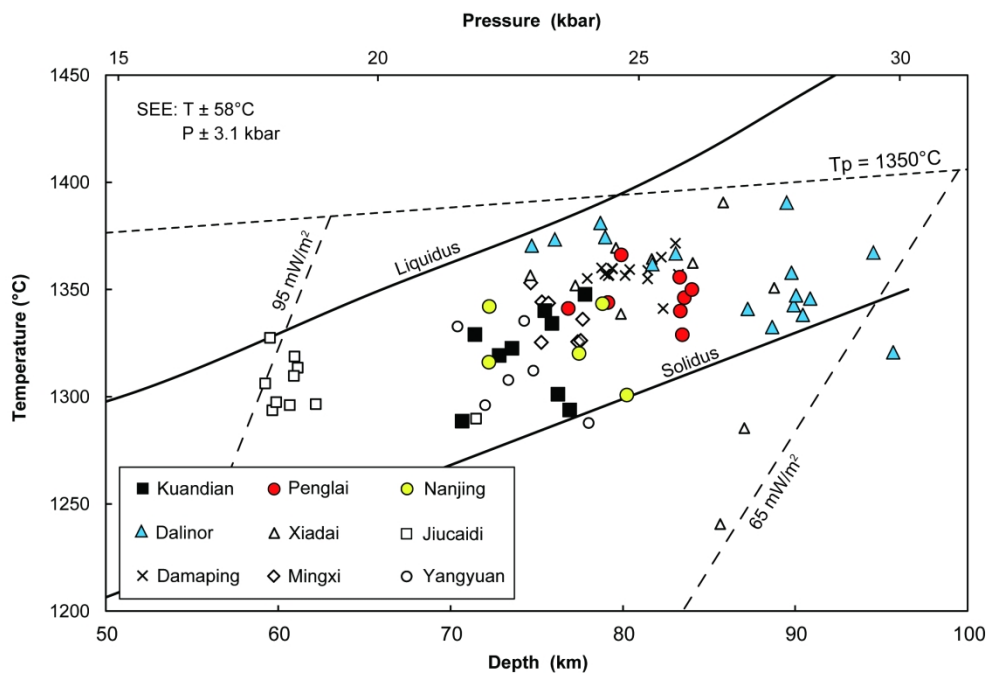


Figure 12 Plots of calculated pressures (P) and temperatures (T) of the clinopyroxene megacrysts. The mantle adiabat for mantle potential temperature (T_p) of 1350 °C, the liquidus and solidus of alkali olivine basalts (Green and Ringwood, 1967) and the continental conductive geotherms of 65 mW/m² and 95 mW/m² modelled using the method of Pollack and Chapman (1977) are also plotted.

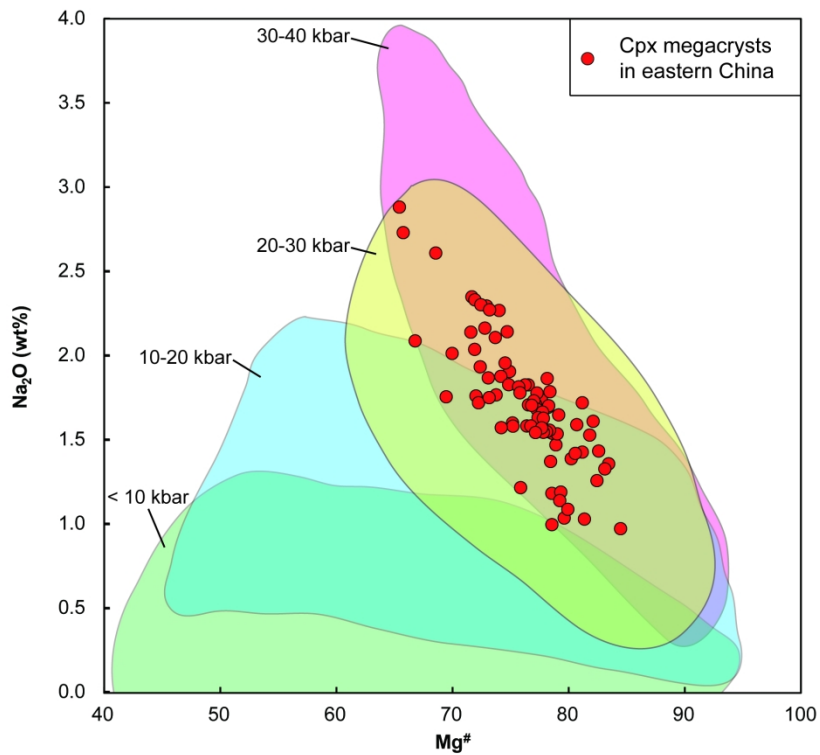


Figure 13 Comparison between clinopyroxene megacrysts in eastern China and experimentally crystallized clinopyroxenes at various pressure ranges (shaded areas) in the Na₂O (wt %)-Mg[#] plot. The data plotted include those of clinopyroxene megacrysts reported in this study and those reported in Sun et al. (2020). The data of experimentally crystallized clinopyroxenes are from LEPR (Library of Experimental Phase Relations; <https://earthchem.org/data-access/>) database.

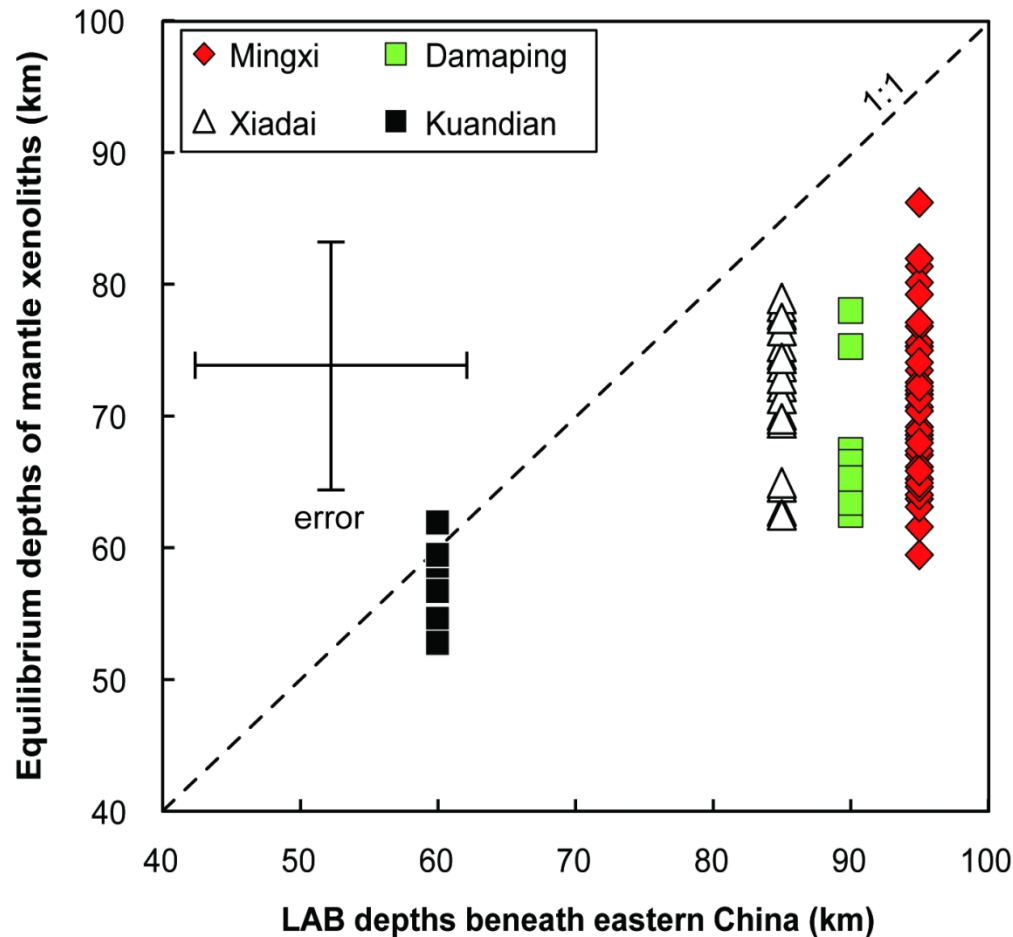


Figure 14 Comparison between the equilibrium pressures (depths) of garnet peridotite and pyroxenite xenoliths co-existing with clinopyroxene megacrysts and the seismically inferred lithosphere-asthenosphere boundary (LAB) depths beneath eastern China. The equilibrium pressures of garnet peridotite and pyroxenite xenoliths include those compiled in Huang & Xu (2010) and those we compiled from the literature (Xu et al., 1998; Qi et al., 1995; Lin et al., 1998). These pressure values were calculated using the geothermobarometers of Nickel & Green (1985) and Brey & Köhler (1990), which were demonstrated to be reliable for garnet-facies xenoliths (Xu et al., 1998). The equilibrium pressures of spinel-facies xenoliths were not compiled because there is no reliable geobarometer for these rocks. The depth values were calculated using an empirical equation: D (km) = 3.04 (km/kbar) \times P (kbar) + 5.35 (km) (Sun et al., 2018), which was generated by estimating the crust (32 km) and lithospheric mantle densities of eastern China. The LAB depths beneath different regions of eastern China were approximated from seismic studies (Chen et al., 2008; Chen, 2009; Li et al., 2013; Shan et al., 2016).

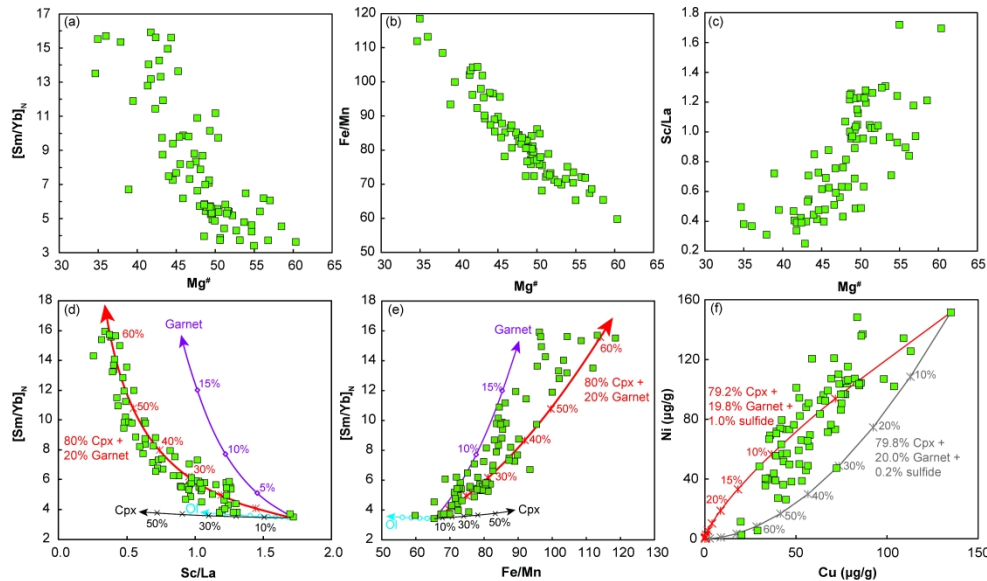


Figure 15 Plots of $Mg^{\#}$ with $[Sm/Yb]_N$ (a), Fe/Mn (b) and Sc/La (c) of melts in equilibrium with the clinopyroxene megacrysts. The effects of fractional crystallization of clinopyroxene, garnet and olivine on melt compositions are modelled in the plots of $[Sm/Yb]_N$ with Sc/La (d) and Fe/Mn (e). The parental melt with lowest $[Sm/Yb]_N$ was approximated as the primitive melt. The effect of immiscible fractionation of sulphide is modelled in the $Cu-Ni$ plot (f) with the parental melt having both highest Cu and Ni as the primitive melt. The partition coefficients of Sm , Yb , Sc and La for clinopyroxene and garnet are from Zack et al. (1997), and those for olivine are from Adam and Green (2006). The partition coefficients of Ni and Cu for clinopyroxene and garnet are from Lee et al. (2012), and those for sulphide are from Pattern et al. (2013). The partition coefficients of Fe and Mn for clinopyroxene, garnet and olivine are from Liu et al. (2008) with $Kd_{(clinopyroxene-Melt)}^{(Fe/Mn)}$ of 0.65.

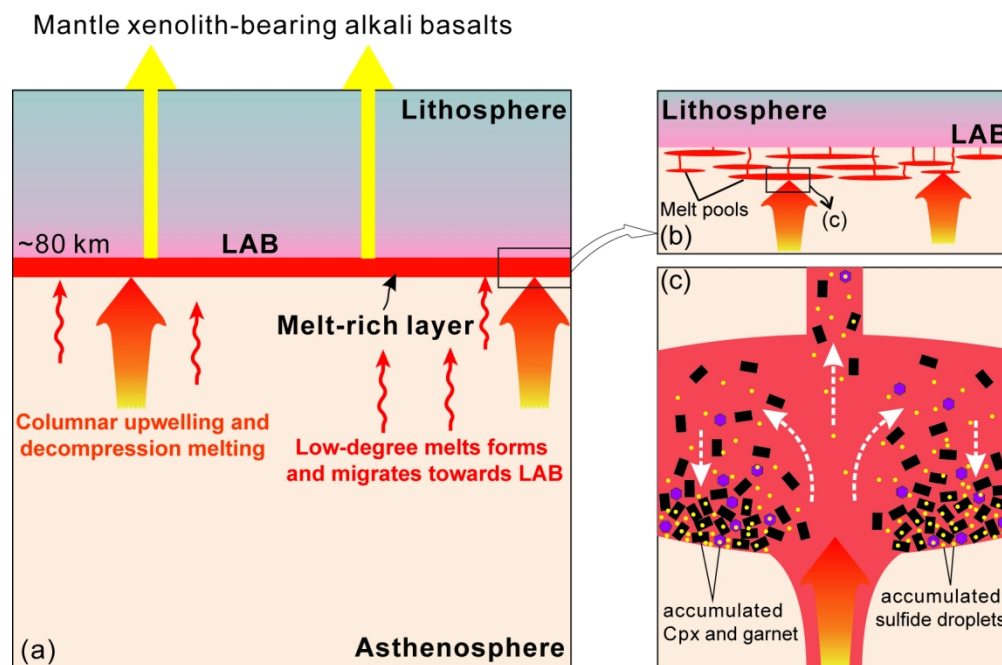


Figure 16 Schematic illustrations for the generation and evolution of Cenozoic basalts in eastern China. Incipient melts that formed at depths (~ 80 -250 km; Green, 2015; Sun et al., 2021) migrate upwards because of their low density and accumulate at the LAB, forming a melt-rich layer with reduced seismic velocity (Chen et al., 2006) (a). This melt-rich layer was inferred to consist of horizontally aligned melt pools embedded in the meltless mantle matrix (e.g., Kawakatsu et al., 2009) (b). These melt pools can provide a stable environment for crystallizing compositionally uniform clinopyroxene and garnet megacrysts concurrent with immiscible fractionation and accumulation of sulphide melt globules (c). Therefore, melts in these melt pools are variably evolved with low $Mg^\#$, low CaO and MnO contents and high Fe/Mn and $[Sm/Yb]_N$. Subsequent pulses of magma aggregation from upwelling mantle columns with more primitive compositions (higher $Mg^\#$) will disturb these melt pools, cause magma mixing and trigger the eruption of magmas carrying clinopyroxene and garnet megacrysts (c).

Table 1 Major and trace element data of clinopyroxene megacrysts from eastern China

Location	<i>Kuandian</i>							
Sample Name	NEC19-89	NEC19-95	NEC19-97	NEC19-102	NEC19-113	KD-CPX-1	KD-CPX-2	KD-CPX-3
LA-ICP-MS (wt %)								
SiO ₂	47.34	49.32	48.44	48.28	46.77	49.48	47.60	48.95
TiO ₂	1.77	1.24	1.01	1.18	1.56	0.93	1.56	0.96
Al ₂ O ₃	9.57	8.93	8.86	9.23	9.46	8.46	9.48	8.70
FeOT	8.72	8.08	7.80	7.48	7.68	7.66	8.71	7.26
MnO	0.14	0.16	0.16	0.15	0.14	0.16	0.15	0.16
MgO	12.40	13.59	15.00	14.37	13.90	14.98	12.69	15.10
CaO	17.60	16.67	16.67	17.30	18.25	16.38	17.48	17.04
Na ₂ O	2.03	1.60	1.65	1.64	1.82	1.56	1.93	1.47
Cr ₂ O ₃	0.002	0.003	0.007	0.001	0.001	0.021	0.000	0.016
Total	99.56	99.58	99.61	99.63	99.59	99.62	99.59	99.64
Mg#	71.70	74.98	77.42	77.41	76.33	77.71	72.19	78.74
LA-ICP-MS (µg/g)								
Sc	20.98	32.52	33.07	31.22	24.98	34.71	23.07	36.45
V	363.44	326.35	311.98	330.57	354.56	306.39	347.62	308.84
Co	47.92	46.68	46.08	45.82	44.40	47.62	48.23	45.37
Ni	115.26	200.44	221.31	180.25	157.10	237.19	131.99	232.95
Cu	1.43	2.46	6.83	1.68	1.28	1.91	1.53	1.69
Zn	46.55	44.28	39.86	39.27	35.83	39.90	45.88	33.40
Ga	18.26	14.29	13.63	14.26	15.87	12.92	17.48	12.40
Sr	103.20	67.91	68.54	76.63	94.34	60.01	96.99	63.10
Y	12.86	13.33	11.90	13.20	12.43	11.77	12.87	12.14
Zr	53.92	34.21	29.85	34.83	48.16	25.47	46.70	26.86
Nb	0.45	0.26	0.30	0.30	0.42	0.20	0.40	0.23
La	2.55	1.51	1.52	1.86	2.36	1.26	2.23	1.42
Ce	9.74	5.81	5.83	7.21	9.13	4.90	8.89	5.61
Pr	1.90	1.20	1.16	1.38	1.76	0.96	1.68	1.07
Nd	11.93	7.60	6.68	8.25	10.73	6.09	10.00	6.54
Sm	4.16	2.46	2.54	3.07	3.50	2.26	3.47	2.26
Eu	1.57	1.09	0.91	1.09	1.34	0.87	1.31	0.89
Gd	4.46	3.47	3.14	4.00	4.11	2.67	4.43	2.90
Tb	0.63	0.54	0.47	0.53	0.62	0.46	0.61	0.46
Dy	3.51	3.15	2.76	3.11	3.27	2.67	3.11	2.60
Ho	0.53	0.49	0.47	0.50	0.52	0.47	0.50	0.48
Er	1.07	1.10	1.17	1.21	0.94	1.11	1.13	1.15
Tm	0.12	0.13	0.12	0.13	0.11	0.13	0.11	0.15
Yb	0.43	0.65	0.76	0.71	0.53	0.75	0.50	0.84
Lu	0.06	0.09	0.09	0.08	0.06	0.09	0.05	0.10
Hf	2.42	1.49	1.34	1.63	2.29	1.08	2.04	1.22
Ta	0.08	0.05	0.05	0.05	0.08	0.03	0.07	0.04
Th	0.04	0.02	0.03	0.03	0.04	0.02	0.04	0.03
<i>P</i> (kbar)	24	22	23	22	21	23	23	22
<i>T</i> (°C)	1294	1319	1334	1323	1289	1340	1301	1329

Table 1 (continued)

Location	<i>Penglai</i>								
	Sample Name	PL19-03	PL19-04	PL19-05	PL19-06A	PL19-06B	PL19-12	PL19-13A	PL19-13B
LA-ICP-MS (wt %)									
SiO ₂	51.26	50.89	49.04	48.50	49.55	51.59	49.61	50.91	49.73
TiO ₂	0.89	0.65	1.03	1.10	0.99	0.96	1.34	0.89	1.02
Al ₂ O ₃	7.81	7.88	8.70	8.95	8.68	7.65	8.78	8.37	7.85
FeOT	7.74	7.75	8.32	8.40	8.48	7.93	9.15	8.38	7.72
MnO	0.14	0.16	0.15	0.14	0.15	0.14	0.14	0.15	0.14
MgO	13.91	15.80	13.80	13.66	13.52	13.36	11.84	13.08	14.91
CaO	16.28	14.94	16.67	16.90	16.36	16.40	16.70	16.07	16.50
Na ₂ O	1.58	1.54	1.90	1.95	1.87	1.58	2.01	1.76	1.73
Cr ₂ O ₃	0.006	0.031	0.003	0.001	0.004	0.005	0.000	0.003	0.009
Total	99.63	99.63	99.61	99.61	99.61	99.62	99.59	99.61	99.62
Mg [#]	76.21	78.40	74.72	74.33	73.97	75.02	69.75	73.56	77.48
LA-ICP-MS (µg/g)									
Sc	19.59	25.11	22.81	21.76	22.44	19.88	19.46	22.24	17.99
V	348.28	303.53	344.72	352.59	340.50	350.14	362.76	338.19	361.47
Co	51.34	51.13	51.75	51.28	52.17	50.86	52.94	52.51	51.22
Ni	239.58	285.49	184.84	167.51	191.97	224.54	128.69	213.97	216.30
Cu	1.77	2.39	1.83	1.86	2.21	1.54	1.49	2.27	1.51
Zn	44.26	44.21	46.09	48.48	49.63	40.79	51.73	48.11	39.82
Ga	13.23	11.61	15.00	15.76	15.00	13.52	17.53	14.10	14.07
Sr	65.51	50.44	72.58	79.99	68.62	65.70	87.09	60.70	76.87
Y	8.27	8.10	9.51	9.57	9.23	8.15	10.05	8.95	7.95
Zr	26.68	16.90	28.78	30.63	27.19	28.14	37.96	23.14	32.62
Nb	0.21	0.16	0.25	0.26	0.19	0.23	0.31	0.19	0.26
La	1.27	0.86	1.35	1.45	1.26	1.30	1.67	1.07	1.51
Ce	4.85	3.17	5.32	5.60	4.78	4.89	6.41	4.12	6.03
Pr	0.89	0.63	1.03	1.08	0.94	0.94	1.18	0.76	1.15
Nd	5.29	3.80	5.98	6.36	5.45	5.34	7.08	4.69	6.61
Sm	1.78	1.34	2.10	2.40	1.98	2.04	2.50	1.82	2.20
Eu	0.70	0.55	0.81	0.86	0.72	0.69	0.93	0.68	0.84
Gd	2.51	1.98	2.57	3.04	2.75	2.37	3.27	2.32	2.45
Tb	0.33	0.29	0.41	0.45	0.40	0.34	0.48	0.36	0.38
Dy	1.90	1.58	2.21	2.41	2.16	1.80	2.44	2.02	2.00
Ho	0.33	0.30	0.39	0.39	0.37	0.33	0.41	0.35	0.32
Er	0.69	0.78	0.83	0.81	0.85	0.67	0.81	0.79	0.69
Tm	0.08	0.09	0.08	0.09	0.09	0.06	0.08	0.08	0.06
Yb	0.35	0.57	0.42	0.51	0.45	0.34	0.35	0.40	0.36
Lu	0.05	0.05	0.06	0.04	0.05	0.05	0.04	0.05	0.03
Hf	1.13	0.73	1.34	1.42	1.22	1.24	1.61	1.02	1.45
Ta	0.04	0.02	0.04	0.04	0.04	0.04	0.06	0.03	0.05
Th	0.02	0.01	0.02	0.03	0.02	0.02	0.03	0.01	0.02
<i>P</i> (kbar)	24	25	26	26	26	24	26	26	24
<i>T</i> (°C)	1348	1366	1346	1340	1350	1341	1329	1356	1344

Table 1 (continued)

Location	<i>Nanjing</i>					<i>Dalinor</i>		
Sample Name	LHPS-01	LHPS-02	LHPS-03	LHPS-05	LHPS-06	DLN19-02	DLN19-03	DLN19-04
LA-ICP-MS (wt %)								
SiO ₂	48.29	49.39	49.76	48.96	47.49	49.21	50.55	49.50
TiO ₂	1.31	1.12	1.35	0.76	1.85	1.33	1.20	1.38
Al ₂ O ₃	9.61	8.98	9.51	8.90	9.68	7.98	7.29	7.93
FeOT	7.87	7.65	7.81	7.02	8.30	8.70	8.90	8.79
MnO	0.15	0.16	0.14	0.16	0.13	0.13	0.13	0.13
MgO	13.00	14.35	12.48	15.81	12.33	13.03	12.46	12.36
CaO	17.57	16.26	16.99	16.64	17.68	16.89	16.91	17.13
Na ₂ O	1.82	1.71	1.57	1.38	2.16	2.29	2.14	2.35
Cr ₂ O ₃	0.003	0.015	0.003	0.028	0.001	0.004	0.002	0.002
Total	99.64	99.64	99.61	99.66	99.63	99.58	99.58	99.58
Mg [#]	74.64	76.97	73.99	80.06	72.59	72.74	71.38	71.47
LA-ICP-MS (µg/g)								
Sc	23.92	36.80	21.92	35.16	16.60	16.92	19.31	19.21
V	336.12	296.31	346.91	299.62	337.86	386.76	371.69	380.26
Co	47.08	46.78	44.67	46.34	43.23	50.96	49.81	49.33
Ni	148.47	237.65	153.48	279.21	88.23	161.18	123.89	117.32
Cu	2.38	3.07	3.11	3.21	1.72	1.99	2.04	1.85
Zn	35.68	44.63	36.76	37.36	56.87	46.32	45.52	46.74
Ga	15.01	13.11	14.85	10.79	17.17	17.56	16.80	18.45
Sr	89.13	62.27	81.96	52.80	115.87	88.97	81.98	96.39
Y	12.78	15.49	10.98	11.13	11.04	8.71	7.94	9.07
Zr	38.79	27.49	36.23	18.83	50.36	46.01	47.30	54.26
Nb	0.47	0.30	0.41	0.20	0.58	0.36	0.36	0.39
La	2.04	1.24	1.89	1.10	2.70	1.73	1.69	1.93
Ce	7.58	4.59	6.63	3.97	10.15	6.86	6.34	7.46
Pr	1.41	0.91	1.21	0.79	1.85	1.30	1.21	1.40
Nd	8.53	5.71	7.09	4.51	11.07	7.62	6.99	8.94
Sm	3.12	2.46	2.55	1.73	3.95	2.66	2.32	2.99
Eu	1.19	1.01	0.99	0.68	1.47	0.99	0.90	1.12
Gd	3.90	3.78	3.29	2.29	4.67	3.37	2.80	3.49
Tb	0.60	0.58	0.44	0.40	0.67	0.45	0.41	0.47
Dy	3.17	3.45	2.57	2.27	3.65	2.28	1.88	2.49
Ho	0.50	0.65	0.42	0.44	0.56	0.36	0.32	0.38
Er	1.21	1.58	0.89	0.93	1.02	0.72	0.59	0.76
Tm	0.15	0.18	0.09	0.15	0.10	0.07	0.07	0.08
Yb	0.52	1.01	0.45	0.76	0.45	0.33	0.30	0.35
Lu	0.07	0.13	0.05	0.12	0.04	0.02	0.03	0.03
Hf	1.69	1.33	1.43	0.87	2.68	2.10	2.03	2.47
Ta	0.08	0.05	0.06	0.04	0.12	0.07	0.06	0.08
Th	0.04	0.02	0.03	0.02	0.05	0.03	0.02	0.03
<i>P</i> (kbar)	24	24	22	22	25	28	27	28
<i>T</i> (°C)	1320	1343	1316	1342	1301	1343	1341	1338

Table 1 (continued)

Location	<i>Dalinor</i>							
Sample	DLN19-05A	DLN19-05B	DLN19-06A	DLN19-06B	DLN19-07	DLN19-08	DLN19-09	DLN19-10
LA-ICP-MS (wt %)								
SiO ₂	49.36	49.06	49.74	49.48	52.51	51.46	50.97	51.16
TiO ₂	1.35	1.57	1.35	1.27	0.51	0.54	1.18	0.47
Al ₂ O ₃	7.71	8.18	7.82	7.85	6.98	7.10	7.51	7.07
FeOT	8.86	9.94	8.72	8.36	6.48	7.28	8.26	6.37
MnO	0.13	0.13	0.13	0.13	0.15	0.16	0.13	0.15
MgO	12.61	10.61	12.73	13.23	16.89	17.43	12.84	17.83
CaO	17.24	17.35	16.80	17.00	14.75	14.14	16.60	15.04
Na ₂ O	2.33	2.73	2.30	2.27	1.25	1.42	2.11	1.35
Cr ₂ O ₃	0.003	0.000	0.002	0.004	0.142	0.086	0.004	0.204
Total	99.58	99.56	99.59	99.59	99.65	99.63	99.60	99.66
Mg [#]	71.72	65.53	72.23	73.83	82.29	81.01	73.48	83.30
LA-ICP-MS (µg/g)								
Sc	17.85	21.25	17.33	18.48	25.31	25.06	17.21	27.36
V	375.77	353.31	379.74	382.75	254.24	264.84	373.51	243.87
Co	49.96	43.05	49.53	48.90	46.49	50.52	49.61	46.93
Ni	126.39	17.76	125.62	142.03	444.29	440.08	184.85	480.75
Cu	1.66	1.24	2.29	1.62	3.72	3.69	1.93	3.59
Zn	47.27	53.76	46.77	44.68	34.52	38.64	46.13	32.13
Ga	17.80	21.25	17.61	17.28	9.56	10.60	16.16	9.00
Sr	96.74	119.86	90.63	91.60	44.79	40.05	84.86	46.89
Y	8.45	9.48	8.61	8.10	6.74	6.89	7.57	6.94
Zr	48.55	85.29	49.13	47.10	12.15	13.67	41.15	11.86
Nb	0.36	0.59	0.38	0.39	0.15	0.14	0.34	0.15
La	1.86	2.28	1.81	1.82	0.88	0.83	1.58	0.92
Ce	7.29	8.83	6.97	6.82	3.22	3.02	6.00	3.28
Pr	1.37	1.65	1.36	1.33	0.60	0.58	1.09	0.59
Nd	8.57	10.38	8.25	7.89	3.71	3.32	6.74	3.41
Sm	2.84	3.32	2.73	2.58	1.23	1.25	2.41	1.30
Eu	0.99	1.15	0.96	0.89	0.43	0.45	0.86	0.48
Gd	3.10	3.74	3.19	2.85	1.49	1.57	2.81	1.62
Tb	0.45	0.52	0.44	0.43	0.23	0.24	0.36	0.24
Dy	2.32	2.67	2.33	2.24	1.34	1.42	2.01	1.52
Ho	0.35	0.38	0.34	0.32	0.26	0.27	0.29	0.26
Er	0.70	0.76	0.71	0.68	0.62	0.69	0.62	0.68
Tm	0.07	0.07	0.07	0.07	0.07	0.09	0.06	0.08
Yb	0.35	0.35	0.29	0.27	0.54	0.49	0.26	0.47
Lu	0.03	0.03	0.03	0.02	0.04	0.06	0.02	0.05
Hf	2.21	3.73	2.22	2.19	0.55	0.60	1.87	0.52
Ta	0.07	0.13	0.08	0.08	0.02	0.02	0.07	0.02
Th	0.03	0.03	0.03	0.02	0.02	0.01	0.02	0.02
<i>P</i> (kbar)	27	30	28	28	23	24	28	24
<i>T</i> (°C)	1332	1321	1346	1347	1370	1374	1358	1381

Table 1 (continued)

Location		<i>Dalinor</i>		<i>Jiucadi</i>	<i>Yangyuan</i>	
Sample	CF14-106	DLN19-01	DLN19-11	PY-JC-02	YYB11-10-1	YYB11-10-2
EMPA (wt %)						
SiO ₂	51.42	51.44	52.01	49.35	48.37	48.84
TiO ₂	0.87	0.87	0.59	1.13	1.77	1.50
Al ₂ O ₃	6.99	7.39	7.02	8.82	9.58	9.65
FeOT	7.66	7.60	6.51	6.92	8.83	8.77
MnO	0.15	0.15	0.15	0.13	0.13	0.13
MgO	15.28	15.22	17.78	14.09	12.63	12.68
CaO	15.65	15.45	14.47	18.13	16.37	16.48
Na ₂ O	1.69	1.70	1.32	1.18	1.76	1.72
Cr ₂ O ₃	0.009	0.018	0.120	0.011	0.006	0.004
Total	99.71	99.84	99.97	99.77	99.46	99.78
Mg [#]	78.04	78.12	82.97	78.38	71.82	72.03
<i>P</i> (kbar)	25	26	23	18	22	22
<i>T</i> (°C)	1361	1367	1373	1296	1297	1308

Table 2 Results of electron microprobe analyses of sulphides

Location	<i>Dalino</i>							
Sample	CF14-106		DLN19-01		DLN19-03		DLN19-11	
Name	n = 12	1 σ	n = 8	1 σ	n = 7	1 σ	n = 5	1 σ
EMPA (wt %)								
As	0.00	0.00	0.01	0.01	0.01	0.02	0.01	0.01
S	38.05	0.44	38.04	0.34	38.11	0.49	37.55	1.41
Pb	0.04	0.05	0.00	0.01	0.02	0.02	0.05	0.05
Co	0.36	0.04	0.39	0.04	0.37	0.07	0.16	0.07
Ni	6.18	0.32	6.45	0.26	2.54	0.23	7.78	0.71
Fe	53.48	0.64	53.75	0.57	57.60	0.41	52.86	0.71
Cu	0.72	0.27	0.33	0.10	0.36	0.19	0.17	0.04
Zn	0.00	0.00	0.00	0.00	0.00	0.00	0.00	0.00
Total	98.82	1.01	98.96	0.56	99.02	0.44	98.58	0.99
Mg# in Cpx	78.21	0.20	78.28	0.36	71.59	0.18	83.11	0.24
Location	<i>Mingxi</i>				<i>Jiucadi</i>			
Sample	DY11-16		PY-DY-09		PY-JC-01II		PY-JC-02	
Name	n = 17	1 σ	n = 10	1 σ	n = 8	1 σ	n = 5	1 σ
As	0.01	0.01	0.01	0.01	0.00	0.01	0.01	0.02
S	38.90	0.27	39.26	0.40	39.26	0.18	39.59	0.31
Pb	0.03	0.03	0.01	0.03	0.05	0.04	0.01	0.02
Co	0.36	0.04	0.39	0.05	0.31	0.11	0.39	0.10
Ni	3.67	0.37	4.92	0.57	3.66	1.00	0.50	0.26
Fe	56.18	0.37	55.26	0.80	56.48	0.92	59.04	0.35
Cu	0.05	0.03	0.03	0.04	0.07	0.12	0.03	0.02
Zn	0.00	0.00	0.00	0.00	0.00	0.00	0.00	0.00
Total	99.19	0.47	99.88	0.35	99.84	0.35	99.58	0.80
Mg# in Cpx	76.06	0.23	76.82	0.22	79.61	0.80	78.38	0.43
Location	<i>Jiucadi</i>		<i>Nanjing</i>				<i>Kuandian</i>	
Sample	PY-JC-04		PY-LHPS-01		PY-LHPS-02		KD-CPX-2	
Name	n = 10	1 σ	n = 20	1 σ	n = 6	1 σ	n = 6	1 σ
As	0.01	0.02	0.00	0.01	0.01	0.02	0.00	0.00
S	39.29	0.54	38.40	0.52	39.21	0.33	39.02	0.52
Pb	0.05	0.05	0.01	0.02	0.00	0.00	0.03	0.05
Co	0.34	0.04	0.33	0.13	0.39	0.03	0.40	0.03
Ni	3.25	0.90	1.97	1.02	4.94	0.28	2.67	0.11
Fe	56.25	1.03	57.48	1.52	55.45	0.17	56.92	0.81
Cu	0.09	0.17	0.02	0.03	0.03	0.04	0.03	0.04
Zn	0.01	0.03	0.00	0.01	0.00	0.00	0.00	0.00
Total	99.29	0.67	98.21	0.95	100.03	0.51	99.08	0.72
Mg# in Cpx	79.06	0.45	74.64	0.38	76.97	0.18	72.19	0.24

Table 2 (Continued)

Location	<i>Penglai</i>		<i>Xiadai</i>				<i>Yangyuan</i>	
Sample	PL19-06		PY-XD-11		PY-XD-08IV		YYB11-10-1	
Name	n = 5	1 σ	n = 6	1 σ	n = 3	1 σ	n = 13	1 σ
As	0.01	0.01	0.00	0.00	0.00	0.00	0.01	0.01
S	38.72	0.30	39.61	0.67	40.89	0.33	39.02	0.22
Pb	0.04	0.04	0.03	0.05	0.00	0.00	0.03	0.04
Co	0.39	0.07	0.12	0.12	0.13	0.06	0.36	0.05
Ni	3.41	0.16	0.73	0.56	2.33	0.46	2.80	0.45
Fe	56.98	0.68	58.84	0.70	55.63	0.74	56.76	0.98
Cu	0.05	0.04	0.02	0.02	0.08	0.02	0.02	0.03
Zn	0.00	0.00	0.02	0.03	0.00	0.00	0.01	0.02
Total	99.60	0.76	99.37	0.57	99.07	0.61	99.01	0.90
Mg# in Cpx	74.33	0.39	65.20	0.37	81.67	0.39	71.82	0.27

Table 3 Major and trace element data of clinopyroxene megacryst-bearing Cenozoic basalts in eastern China

Location	<i>Kuandian</i>							
Sample Name	NEC19-89	NEC19-95	NEC19-97	NEC19-102	NEC19-113	NEC19-94	NEC19-103	NEC19-109
ICP-OES (wt %)								
SiO ₂	48.28	48.67	48.53	48.84	49.70	48.54	48.63	49.74
TiO ₂	2.55	2.52	2.32	2.31	2.29	2.27	2.76	2.31
Al ₂ O ₃	14.88	12.94	14.51	14.31	14.75	14.49	12.72	14.37
FeO _T	11.30	11.92	10.65	10.33	10.76	10.64	12.38	10.91
MnO	0.17	0.19	0.16	0.16	0.16	0.16	0.19	0.17
MgO	6.52	8.01	7.15	8.84	8.10	6.99	8.44	7.91
CaO	7.11	7.12	7.17	7.79	7.12	7.13	7.73	7.80
Na ₂ O	4.71	3.37	4.46	3.62	3.88	4.34	3.15	3.83
K ₂ O	3.08	2.92	2.81	2.24	2.32	2.83	2.58	2.36
P ₂ O ₅	0.71	0.30	0.63	0.44	0.33	0.59	0.19	0.43
Total	99.30	97.96	98.39	98.89	99.42	97.99	98.76	99.83
Mg [#]	53.31	57.09	57.06	62.91	59.83	56.54	57.46	58.95
CaO/Al ₂ O ₃	0.48	0.55	0.49	0.54	0.48	0.49	0.61	0.54
ICP-MS (µg/g)								
Li	8.28	11.18	9.17	6.98	5.43	9.35	10.54	8.51
Sc	14.33	15.78	15.75	19.69	17.51	15.95	18.13	18.14
V	149.1	165.3	157.2	180.1	153.6	153.1	181.3	164.3
Cr	115.9	212.1	216.2	327.5	174.7	204.7	222.1	202.3
Mn	1321	1469	1256	1262	1232	1273	1478	1314
Co	41.75	46.89	42.04	48.86	46.12	41.00	49.33	46.14
Ni	107.0	184.5	159.9	272.0	191.8	154.8	171.7	180.9
Cu	29.95	22.00	29.48	46.47	28.55	30.99	14.04	36.75
Zn	148.1	158.3	138.4	107.7	120.8	138.9	157.0	125.0
Ga	23.33	22.20	23.28	19.57	21.35	23.52	20.44	21.05
Rb	48.66	46.46	44.56	47.94	31.19	49.16	37.22	34.88
Sr	926.9	1077	914.8	679.0	698.2	915.5	1016	747.6
Y	21.56	15.74	20.16	19.59	14.70	19.90	14.98	18.85
Zr	308.2	353.7	299.0	221.1	248.2	308.5	336.4	260.2
Nb	72.98	77.18	67.56	46.30	54.74	70.07	75.80	57.48
Cs	0.53	0.45	0.54	0.46	0.37	0.55	0.36	0.39
Ba	732.7	673.9	568.2	534.4	454.6	566.0	651.6	465.5
La	41.84	24.41	37.80	27.76	21.29	36.76	16.95	26.36
Ce	82.65	49.22	74.39	54.22	41.07	72.30	35.70	52.61
Pr	9.50	5.92	8.52	6.22	4.74	8.32	4.49	6.15
Nd	37.96	24.58	34.30	25.29	19.61	33.64	20.02	25.45
Sm	8.05	5.65	7.34	5.60	4.53	7.23	4.97	5.87
Eu	2.63	2.36	2.55	1.97	1.75	2.49	2.17	2.15
Gd	6.95	4.97	6.50	5.31	4.32	6.32	4.52	5.47
Tb	0.98	0.74	0.91	0.78	0.63	0.89	0.67	0.78
Dy	4.80	3.59	4.47	4.06	3.26	4.42	3.40	4.07
Ho	0.84	0.63	0.80	0.75	0.60	0.77	0.61	0.75
Er	1.97	1.51	1.85	1.93	1.50	1.83	1.46	1.78

Table 3 (continued)

Location		<i>Kuandian</i>						
Sample Name	NEC19-89	NEC19-95	NEC19-97	NEC19-102	NEC19-113	NEC19-94	NEC19-103	NEC19-109
Tm	0.24	0.19	0.23	0.26	0.19	0.23	0.20	0.23
Yb	1.33	1.11	1.29	1.50	1.12	1.29	1.16	1.33
Lu	0.18	0.16	0.18	0.23	0.15	0.18	0.16	0.19
Hf	6.77	7.72	6.55	4.95	5.48	6.64	7.40	5.72
Ta	4.31	4.93	4.09	2.73	3.31	4.17	4.58	3.50
Pb	4.10	3.07	3.86	3.87	3.21	3.90	2.77	3.43
Th	5.64	4.84	5.51	4.29	4.24	5.61	3.43	4.26
U	1.46	1.02	1.28	1.09	1.18	1.25	1.16	1.08
[Sm/Yb] _N	6.73	5.67	6.33	4.15	4.50	6.24	4.78	4.90
^a Fe/Mn	66.28	64.33	65.98	64.05	66.27	65.61	65.53	63.75
^b Fe/Mn	66.49	63.08	65.91	63.59	67.92	65.00	65.10	64.52

Location		<i>Penglai</i>						
Sample Name	PL19-03	PL19-04	PL19-05	PL19-06	PL19-12	PL19-13	PL19-14	PL19-15
ICP-OES (wt %)								
SiO ₂	45.21	48.13	48.02	47.83	45.19	47.33	45.74	45.21
TiO ₂	3.50	3.38	3.36	3.34	3.57	3.52	3.40	3.44
Al ₂ O ₃	12.80	13.87	13.60	14.09	12.68	14.24	12.53	12.57
FeO _T	13.61	13.24	13.12	13.36	13.88	13.49	13.70	13.42
MnO	0.17	0.14	0.14	0.15	0.17	0.15	0.17	0.17
MgO	7.09	5.24	5.29	5.25	7.07	5.31	7.12	7.03
CaO	8.53	7.35	7.09	7.21	8.27	7.20	8.31	8.46
Na ₂ O	4.11	3.46	3.62	3.09	4.14	3.00	4.75	5.05
K ₂ O	1.22	1.54	1.36	3.10	0.99	3.19	1.25	0.99
P ₂ O ₅	0.89	0.76	0.78	0.76	0.91	0.78	0.81	0.92
Total	97.13	97.10	96.36	98.17	96.85	98.21	97.78	97.26
Mg [#]	50.80	43.93	44.38	43.77	50.21	43.82	50.70	50.93
CaO/Al ₂ O ₃	0.67	0.53	0.52	0.51	0.65	0.51	0.66	0.67
ICP-MS (µg/g)								
Li	8.15	10.28	9.90	11.09	6.99	11.15	7.18	8.43
Sc	11.46	10.71	10.59	10.50	10.92	10.36	11.39	11.58
V	195.1	173.8	173.6	172.7	195.6	172.6	192.9	189.2
Cr	187.6	61.86	67.80	67.73	106.6	58.55	168.5	161.2
Mn	1272	1097	1108	1151	1286	1155	1265	1293
Co	48.26	41.65	42.83	43.86	50.86	43.30	47.66	48.82
Ni	184.1	91.16	106.4	92.06	138.1	85.91	160.2	126.2
Cu	35.99	30.10	21.07	31.51	34.60	33.09	33.17	29.72
Zn	170.2	179.2	178.0	180.6	176.1	179.6	169.2	188.2
Ga	26.75	26.56	26.13	27.27	26.78	27.35	26.51	26.56
Rb	38.45	17.76	21.04	45.08	36.40	48.60	43.40	49.89
Sr	1148	1066	1021	1068	1145	1053	1041	1222

Table 3 (continued)

Location	<i>Penglai</i>							
Sample Name	PL19-03	PL19-04	PL19-05	PL19-06	PL19-12	PL19-13	PL19-14	PL19-15
Y	23.10	21.40	19.89	19.50	21.98	20.60	21.88	23.34
Zr	357.3	320.9	319.4	312.4	364.8	314.6	359.7	359.9
Nb	97.64	86.01	85.70	83.09	100.1	83.52	99.06	98.74
Cs	0.73	3.25	2.78	0.33	0.71	0.72	0.56	0.64
Ba	561.0	590.5	575.9	591.7	543.4	593.7	530.0	558.9
La	50.71	44.07	40.17	40.29	48.76	42.00	46.23	52.79
Ce	99.23	85.87	79.33	79.31	95.91	83.08	92.03	103.11
Pr	11.66	10.24	9.41	9.41	11.29	9.87	10.91	12.02
Nd	46.55	40.59	38.13	37.93	44.84	39.73	43.75	47.64
Sm	10.42	9.45	8.87	8.89	10.35	9.31	10.14	10.76
Eu	3.19	2.96	2.79	2.84	3.14	2.92	3.05	3.25
Gd	9.59	8.82	8.34	8.23	9.61	8.77	9.23	10.03
Tb	1.18	1.07	1.04	1.02	1.15	1.06	1.14	1.21
Dy	5.50	5.06	4.78	4.74	5.25	4.91	5.29	5.56
Ho	0.93	0.85	0.81	0.79	0.89	0.83	0.88	0.92
Er	2.01	1.88	1.81	1.74	1.95	1.83	1.94	2.01
Tm	0.22	0.21	0.20	0.19	0.21	0.20	0.21	0.22
Yb	1.07	1.06	0.99	0.96	1.04	1.01	1.03	1.07
Lu	0.14	0.13	0.12	0.12	0.12	0.12	0.13	0.13
Hf	7.75	6.98	7.00	6.88	7.90	6.87	7.71	7.71
Ta	5.93	5.21	5.21	5.17	6.00	5.12	5.90	5.94
Pb	3.91	4.08	3.94	4.58	3.88	4.31	3.87	3.73
Th	6.71	6.00	5.86	5.98	6.62	5.98	6.52	6.85
U	1.83	1.67	1.72	1.49	1.91	1.50	1.84	1.80
[Sm/Yb] _N	10.77	9.88	9.96	10.23	11.08	10.25	10.92	11.21
^a Fe/Mn	81.81	91.65	90.96	88.09	82.47	88.21	81.97	80.05
^b Fe/Mn	83.15	93.82	92.01	90.15	83.91	90.76	84.21	80.69

Location	<i>Penglai</i>		<i>Dalinor</i>					
Sample Name	PL19-16	PL19-17	DLN19-01	DLN19-02	DLN19-03	DLN19-04	DLN19-05	DLN19-06
ICP-OES (wt %)								
SiO ₂	45.19	45.35	44.97	42.76	42.80	42.24	43.25	43.52
TiO ₂	3.41	3.53	3.56	3.76	3.71	3.87	3.76	3.85
Al ₂ O ₃	12.86	12.73	12.06	11.54	11.75	11.63	11.87	11.92
FeO _T	13.61	13.47	13.17	13.47	13.17	13.45	13.38	13.74
MnO	0.17	0.17	0.18	0.18	0.17	0.18	0.18	0.18
MgO	6.55	6.94	10.01	9.44	9.30	8.95	9.35	9.36
CaO	8.34	8.25	9.87	9.46	9.14	9.02	9.21	9.32
Na ₂ O	4.99	4.64	4.03	4.10	4.30	4.43	3.97	4.44
K ₂ O	1.06	1.07	2.59	2.79	2.88	3.04	3.05	3.03
P ₂ O ₅	0.89	0.92	0.96	0.99	1.04	1.07	1.10	1.08
Total	97.07	97.08	101.40	98.49	98.27	97.88	99.11	100.45

Table 3 (continued)

Location	<i>Penglai</i>				<i>Dalinor</i>			
Sample Name	PL19-16	PL19-17	DLN19-01	DLN19-02	DLN19-03	DLN19-04	DLN19-05	DLN19-06
Mg [#]	48.79	50.50	60.06	58.12	58.30	56.86	58.06	57.44
CaO/Al ₂ O ₃	0.65	0.65	0.82	0.82	0.78	0.78	0.78	0.78
ICP-MS (µg/g)								
Li	8.12	8.36	7.54	7.79	8.09	8.53	5.56	8.46
Sc	10.60	10.84	17.75	15.41	14.88	13.82	14.20	14.67
V	191.0	194.2	267.7	266.2	263.4	265.7	255.5	263.0
Cr	93.55	122.5	165.9	115.4	107.6	91.87	104.7	102.1
Mn	1263	1345	1360	1363	1369	1391	1335	1371
Co	46.90	50.38	59.87	60.73	61.90	61.10	59.06	60.65
Ni	126.8	122.1	213.7	181.6	187.5	164.2	169.1	168.7
Cu	32.63	30.71	65.37	50.29	51.67	46.71	44.39	47.03
Zn	173.5	175.0	148.1	162.5	162.4	172.1	161.5	169.4
Ga	27.09	27.38	22.92	23.54	23.87	24.82	23.75	24.29
Rb	59.08	42.47	46.01	51.83	55.26	57.48	54.97	55.82
Sr	1074	1152	895.4	980.0	1019	1072	994.6	1056
Y	22.61	23.03	24.57	24.51	24.71	25.03	24.16	25.08
Zr	363.0	369.2	269.8	290.6	295.2	310.9	294.0	307.1
Nb	100.1	102.6	81.32	90.59	92.78	98.73	93.26	96.86
Cs	0.61	0.71	0.53	0.56	0.58	0.63	0.59	0.61
Ba	518.6	552.0	679.9	765.8	805.7	836.6	788.4	822.9
La	50.58	52.85	48.48	53.97	55.75	58.71	55.81	58.47
Ce	99.77	103.35	94.18	103.87	107.03	112.09	106.50	112.31
Pr	11.75	12.02	11.20	12.21	12.64	13.07	12.40	13.37
Nd	46.16	47.73	44.76	48.44	49.77	52.26	49.36	52.06
Sm	10.53	10.83	10.12	10.96	11.07	11.62	10.98	11.49
Eu	3.18	3.27	3.03	3.28	3.34	3.47	3.28	3.46
Gd	9.81	10.09	9.55	10.20	10.32	10.88	10.29	10.81
Tb	1.18	1.19	1.15	1.21	1.23	1.27	1.21	1.27
Dy	5.42	5.56	5.52	5.59	5.66	5.90	5.62	5.83
Ho	0.90	0.92	0.98	0.96	0.97	1.00	0.96	1.00
Er	1.99	1.99	2.28	2.24	2.23	2.25	2.17	2.26
Tm	0.22	0.22	0.27	0.26	0.25	0.24	0.25	0.25
Yb	1.03	1.06	1.44	1.34	1.30	1.28	1.25	1.26
Lu	0.13	0.13	0.18	0.17	0.16	0.16	0.16	0.16
Hf	7.83	7.87	5.92	6.36	6.43	6.72	6.31	6.67
Ta	6.05	6.13	4.72	5.28	5.33	5.70	5.33	5.55
Pb	4.01	3.97	3.08	3.36	3.90	3.69	3.50	3.62
Th	7.02	6.82	6.43	7.08	7.27	7.75	7.33	7.73
U	1.90	1.79	1.73	1.88	1.96	2.07	1.95	2.06
[Sm/Yb] _N	11.40	11.37	7.81	9.08	9.44	10.11	9.74	10.13
^a Fe/Mn	81.32	78.00	72.70	75.52	75.73	76.65	74.77	75.64
^b Fe/Mn	83.77	77.83	75.27	76.85	74.78	75.16	77.85	77.89

Table 3 (continued)

Location	<i>Dalinor</i>		<i>Nanjing</i>				
Sample Name	DLN19-07	DLN19-08	LHPS16-01	LHPS16-02	LHPS16-03	LHPS16-05	LHPS16-06
ICP-OES (wt %)							
SiO ₂	44.19	44.01	47.05	46.93	45.93	46.11	46.56
TiO ₂	3.70	3.70	2.21	2.18	2.15	2.12	2.15
Al ₂ O ₃	12.07	11.80	15.09	15.08	14.54	14.57	14.81
FeO _T	13.32	13.39	9.85	9.85	9.80	9.61	9.99
MnO	0.18	0.18	0.15	0.15	0.15	0.15	0.15
MgO	9.45	9.72	7.05	7.19	7.39	7.03	7.13
CaO	9.52	9.40	7.52	7.38	7.79	7.49	7.51
Na ₂ O	4.12	3.99	5.52	5.29	5.46	4.79	5.55
K ₂ O	2.85	2.80	2.76	2.80	2.51	3.66	3.33
P ₂ O ₅	0.98	1.00	0.81	0.80	0.78	0.81	0.82
Total	100.38	100.00	98.01	97.65	96.49	96.35	98.01
Mg [#]	58.42	58.97	58.64	59.12	59.89	59.16	58.57
CaO/Al ₂ O ₃	0.79	0.80	0.50	0.49	0.54	0.51	0.51
ICP-MS (µg/g)							
Li	7.82	7.64	9.79	9.56	8.85	9.00	8.94
Sc	15.91	15.76	15.09	15.08	16.42	14.51	16.80
V	266.9	269.7	143.8	143.1	153.1	143.0	141.7
Cr	125.8	129.7	212.9	290.6	244.7	192.2	216.7
Mn	1363	1375	1217	1209	1214	1165	1210
Co	60.96	63.41	39.36	38.95	39.77	37.98	39.18
Ni	197.3	211.9	159.8	157.0	161.6	154.3	159.0
Cu	54.93	53.88	34.0	32.96	55.85	57.78	28.46
Zn	156.1	157.5	139.1	139.2	137.1	135.5	137.7
Ga	23.61	23.17	24.83	24.69	24.20	24.32	24.72
Rb	51.61	51.02	51.98	41.96	49.03	58.72	45.65
Sr	956.0	945.3	1011	1071	1059	1120	1059
Y	24.29	24.05	22.19	22.21	21.78	21.91	22.05
Zr	281.6	280.3	278.8	281.3	271.2	277.6	276.5
Nb	87.17	87.02	88.12	91.93	85.57	87.86	86.68
Cs	0.55	0.55	0.82	0.53	0.78	0.71	0.79
Ba	765.1	769.4	522.2	529.4	514.8	518.7	508.5
La	52.01	52.28	52.98	53.45	51.52	53.06	53.23
Ce	99.69	101.04	95.42	95.55	92.10	94.39	94.70
Pr	11.70	11.76	10.34	10.38	10.06	10.27	10.31
Nd	47.46	47.17	40.27	39.98	38.75	39.60	39.63
Sm	10.46	10.52	8.22	8.21	8.06	8.11	8.08
Eu	3.15	3.14	2.66	2.62	2.58	2.58	2.61
Gd	10.03	10.02	6.52	6.45	6.63	6.63	6.68
Tb	1.20	1.18	0.97	0.97	0.95	0.95	0.94
Dy	5.51	5.57	5.04	4.97	4.87	4.87	4.82
Ho	0.97	0.98	0.85	0.84	0.82	0.82	0.83
Er	2.30	2.27	1.98	2.00	1.95	1.98	2.00

Table 3 (continued)

Location	<i>Dalinor</i>		<i>Nanjing</i>				
Sample Name	DLN19-07	DLN19-08	LHPS16-01	LHPS16-02	LHPS16-03	LHPS16-05	LHPS16-06
Tm	0.26	0.26	0.24	0.24	0.22	0.22	0.22
Yb	1.37	1.32	1.26	1.29	1.27	1.29	1.32
Lu	0.17	0.17	0.16	0.16	0.15	0.16	0.16
Hf	6.21	6.19	6.17	6.06	5.92	5.99	5.99
Ta	5.06	5.06	6.04	6.10	5.40	5.41	5.36
Pb	3.26	3.27	3.51	3.78	4.54	4.40	3.50
Th	6.81	6.84	7.00	7.25	6.86	7.07	7.06
U	1.83	1.85	2.05	2.07	1.93	2.05	1.99
[Sm/Yb] _N	8.47	8.83	7.22	7.07	7.03	6.98	6.81
^a Fe/Mn	74.45	74.57	64.61	64.47	64.54	65.45	64.85
^b Fe/Mn	75.98	75.69	62.91	63.34	62.74	64.14	64.16

^a Calculated using MnO (wt %) measured by ICP-OES; ^b Calculated using Mn (μg/g) measured by ICP-MS.